

1 Challenges and Opportunities of Superhydrophobic/Superamphiphobic Coatings in Real Applications

Maxime Paven, Lena Mammen, Doris Vollmer

Max-Planck Institute for Polymer Research, Mainz, Germany

E-mail: vollmerd@mpip-mainz.mpg.de

Contamination of surfaces with organic compounds and biological residues still represents a broad challenge ranging from industry and medicine to our daily live. Superhydrophobic coatings are exceptionally water repellent and have self-cleaning properties. Water drops roll off when tilting the surface by a few degrees. However, low surface tension liquids like oils and other organic contaminants easily adhere to superhydrophobic surfaces. Recently developed superamphiphobic coatings may prevent this problem. Superamphiphobic coatings could not only prevent wetting of surfaces by oil but also delay deposition of biological material such as cells, proteins and bacteria. In this chapter we discuss the wetting behaviour of superhydrophobic and superamphiphobic surfaces. We address topics beyond the fabrication, characterization and optimization process of super-liquid repellent surfaces and present possible application fields, ranging from industry to medicine. Still the durability and the long-term stability of superhydrophobicity/superamphiphobicity present major challenges, limiting their industrial use

1.1 Wetting

Understanding wetting of solids by liquids is essential in many biological, medical and industrial processes, ranging e.g. from artificial tissue engineering to practical applications like biofouling, non-fogging coatings, fog harvesting, or self-cleaning textiles. Especially surfaces with high liquid repellency, often inspired by nature, have promising applications.

The wetting behaviour of an ideal flat and chemically homogeneous surface can be described by the Young equation. It can be derived by balancing the interfacial forces at a three-phase contact line: ¹

$$\cos \theta = \frac{\gamma_S - \gamma_{SL}}{\gamma_L} \quad (1)$$

Here γ_L , γ_S and γ_{SL} are the liquid-gas, solid-gas and solid-liquid interfacial tensions. In reality, the surface is never completely flat and chemically homogeneous. To account for this non-ideality, we call the contact angle ϑ measured on a flat surface the material contact angle instead of Young contact angle. ϑ can be estimated by eye or quantified by optical microscopy (Figure 1.1). Depending on the value of ϑ one distinguishes between hydrophilic ($\vartheta < 90^\circ$, $\gamma_S > \gamma_{SL}$) and hydrophobic ($\vartheta > 90^\circ$, $\gamma_S < \gamma_{SL}$) surfaces (Figs. 1a,b). For $\gamma_S = \gamma_{SL} + \gamma_L$ the liquid completely wets the surface ($\vartheta = 0^\circ$), whereas for $\gamma_S < \gamma_{SL} + \gamma_L$ a finite contact angle is formed. A hydrophilic surface is also called a high energy surface. The surface energy can be lowered by coating a surface e.g. with fluorinated molecules. In that case, contact angles of about 120° have been reported on a smooth homogeneous surface^{2, 3}.

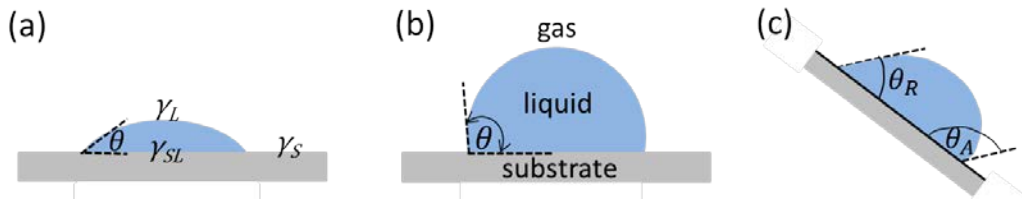


Figure 1.1 Sketch of a sessile drop on a surface. The material contact angle ϑ can be determined at the three-phase contact line of liquid, surface and vapour. (a) Hydrophilic substrate, (b) Hydrophobic substrate, (c) The difference between the advancing ϑ_A and receding ϑ_R material contact angle determines the contact angle hysteresis.

The material's contact angle describes wetting at the macroscopic scale, meaning 0.1-1 μm away from the real wetting line. However, very close to the wetting line i.e. in a range of 1-100 nm surface forces, like van der Waals or electrostatic double-layer forces come into play, leading to a deviating microscopic contact angle⁴.

In reality a completely smooth and chemically homogeneous surface does not exist. The drop will start to move as soon as the surface is tilted above a certain angle, the so termed roll-off angle α (Figure 1.1c). Tilting causes that the contact angles at the front and rear side of the drop differ. ϑ_A denotes the angle at the front side when the drops starts to advance. Correspondingly, ϑ_R denotes the angle at the rear when the rear side of the drop starts to advance. The reason that drop motion requires a certain tilting angle is caused by pinning of the drop on chemical inhomogeneities or surface protrusions. On a smooth surface high adhesion often prevents that the drop rolls-off. Alternatively, the advancing material contact angle ϑ_A can be determined by increasing the volume of a liquid drop until the three-

phase contact line starts to advance. Correspondingly, to receive the receding material contact angle ϑ_A the volume is reduced until the three-phase contact line recedes. The difference, $\vartheta_A - \vartheta_R$, is called contact angle hysteresis.

1.1.1 Rough surface: Wenzel's and Cassie's models

Wenzel suggested that the wetting behaviour of a rough and smooth surface are related: *"It is only necessary to apply the fact that, within a measured unit area on a rough surface, there is actually more surface, and in that sense therefore a greater intensity of surface energy, than in the same measured unit area on a smooth surface"*[4]. Based on the assumption of thermodynamic equilibrium and complete wetting of the surface's protrusions, Wenzel generalized the Young equation towards rough surfaces⁵:

$$\cos \Theta_W = r \cdot \cos \theta, \quad r \geq 1 \text{ and } |\cos \Theta_W| \leq 1 \quad (2)$$

Θ_W is the apparent contact angle on a rough surface, r is the total surface area divided by the projected surface area, and ϑ is the material contact angle on a smooth surface with the same chemical composition (Figure 1.2a). In the following, we use the term apparent contact angle for drops on rough surfaces to distinguish those from the angle on its smooth counterpart. According to the Wenzel model, surface roughness increases the surface's hydrophobicity or hydrophilicity. The apparent contact angle decreases on a hydrophilic surface and increases on a hydrophobic surface.

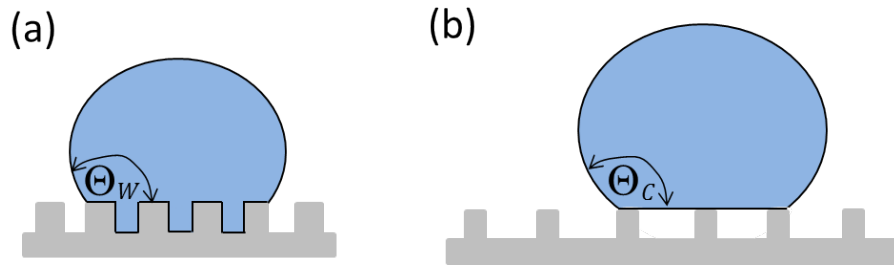


Figure 1.2 A sessile liquid drop resting on a rough surface in the fully wetted Wenzel state (a) and in the composite Cassie-Baxter state (b) respectively.

However, for hydrophobic surfaces that are very rough (large r) the Wenzel formula predicts a total drying of the surface ($\Theta_W = 180^\circ$) which is not physical due to the lack of contact between the drop and the substrate⁶. In this case it is energetically favourable that the liquid drop partially rests on air pockets and partially on top of the protrusions (Figure 1.2b). This composite state is referred to as the Cassie or Cassie-Baxter state. In thermodynamic equilibrium the apparent contact angle Θ_C on a composite surface consisting of two materials Θ_C can be calculated with the Cassie-Baxter equation⁷:

$$\cos \Theta_c = f_1 \cos \theta_1 + f_2 \cos \theta_2 \quad (3)$$

Here f_1 and f_2 are the fractional surface areas of the two components being in contact with the liquid drop and ϑ_1 and ϑ_2 are the corresponding material contact angles. The Cassie equation (Eq. 1.3) is derived from a minimization of the total free energy considering all interfacial and surface energies. If the second component is air ($f_2 = 1 - f_1 = f_{air}$; $\vartheta_2 = 180^\circ$; $\vartheta_1 = \vartheta$), the Cassie equation can be rewritten as:

$$\cos \Theta_c = f (1 + \cos \theta) - 1; \text{ and } f_1 \equiv f \quad (4)$$

The adhesion of a drop on a surface differs significantly for the Wenzel or Cassie state, despite the fact that in both cases the apparent contact angle can exceed 150° . In the Wenzel state, adhesion is large due to the extended contact line. In general, a drop cannot roll-off but remains pinned on the surface even if $\alpha = 90^\circ$. On the contrary, if the contact line is broken, the drop can move easily. This holds for a drop in the Cassie state. Adhesion is low if the drop partially rests on air cushions ($f_2 = f_{air}$). This is an important property for the preparation of self-cleaning surfaces.

Both, the Wenzel and the Cassie equation predict exactly one apparent contact angle for a certain surface topography and surface material. Contrarily, the apparent contact angle can vary greatly from experiment to experiment, as its value depends on the way the drop is deposited and on the exact position on the surface. This dependence of the apparent contact angle on details of the experimental procedure and surface properties is caused by roughness and surface inhomogeneities, as these cause pinning of the contact line at certain positions^{4, 8}. The apparent contact angle can take every value between the apparent receding and apparent advancing contact angle, $\Theta_r^{app} \leq \Theta^{app} \leq \Theta_a^{app}$.

In the following we will not discuss the advancing and receding contact angles on a flat surface. Therefore, we will delete the indices “app”, i.e. Θ_a and Θ_r refer to the apparent advancing and, respectively, receding contact angle on a rough surface. Often it is difficult to decide whether a drop is in the Wenzel or in the Cassie state as the contact angle can be large in both cases. In general a drop rolls-off much easier in the Cassie state than in the Wenzel state. However, the roll-off angle can also exceed 20° for drops in the Cassie state. Furthermore, a drop can be partially in the Wenzel and partially in the Cassie state.

1.1.2 Laser scanning confocal microscopy (LSCM)

Detailed information on the shape of the drop-air and drop-substrate interface can be obtained by laser scanning confocal microscopy, in the following referred to as LSCM (Figure 1.3). LSCM renders it possible to image the interface between a drop

and a substrate with a resolution of 250 nm in horizontal and 700 nm in vertical direction. In this case the substrate needs to be transparent. To determine the drop contour and the contact angles, data analysis is easier if both, the water drop and the substrate, are fluorescently labelled. It is important that the dyes are not interfacial active. If more than one dye is used, care needs to be taken that the emission wavelengths of the dyes do not overlap. If the LSCM has more than one detector, the reflection of light from the interfaces with sufficient difference of the refractive indices can be measured simultaneously. No reflection is visible if the difference of the reflective indices, Δn , is too low, here for $\Delta n < 0.1$. To quantify the thickness of the air cushion or the height of the pillars, the indices of refraction of the objective and the medium should be identical. Otherwise, the heights need to be corrected by the refractive indices of the components. A dry objective allows determining the coordinates of the water-air interface, to measure the thickness of the air layer and to determine the apparent contact angle with high accuracy.

Micropillar arrays, e.g. made from poly-dimethylsilane (PDMS) or SU8, a commonly used epoxy-based negative photoresist, are well-suited model systems to obtain fundamental understanding on the wetting dynamics. Figure 1.3a displays a sketch of a water drop in the Wenzel and, Figure 1.3b, in the Cassie state. A 2D-cross section along the x-z axis shows water (blue) in contact with the PDMS pillars (yellow) and air (black). The magenta lines mark the reflection of light from the pillar-air, and air-water interface. No reflection is visible from the water-PDMS interface due to the low difference of the refractive indices, $n_{H_2O} = 1.33$ and $n_{PDMS} = 1.45$. The height of the pillars appears too short by a factor proportional to $1/n$. Therefore, artificial pillars are inserted in Figure 1.3d. The height of the pillars was taken from SEM images.

In the Wenzel state, the water drop follows the topography of the pillars, reflected in a periodic step profile (Figure 1.3c) ⁹. At the three-phase contact line the water-air interface sharply bends upwards. The tangent at the three-phase contact line to the drop gives the apparent contact angle. Independent of the topography, locally it is energetically favourable for a drop to assume its material contact angle, i.e. $\vartheta = 109^\circ$ in case of PDMS. Furthermore, a drop tends to minimize its contact area with the surface to minimize its total surface energy. These competing restrictions cause a bending of the liquid surface close to the three-phase contact line. As a results the apparent contact angle varies along the three-phase contact line (Figure 1.3d,e). The local maxima are due to the vertical slopes and the rim of the pillars' top surface. The minima correspond to the inter-pillar valleys and the flat area on the pillars' top surface, resulting in variations of the apparent contact angle by up to 20° ⁹.

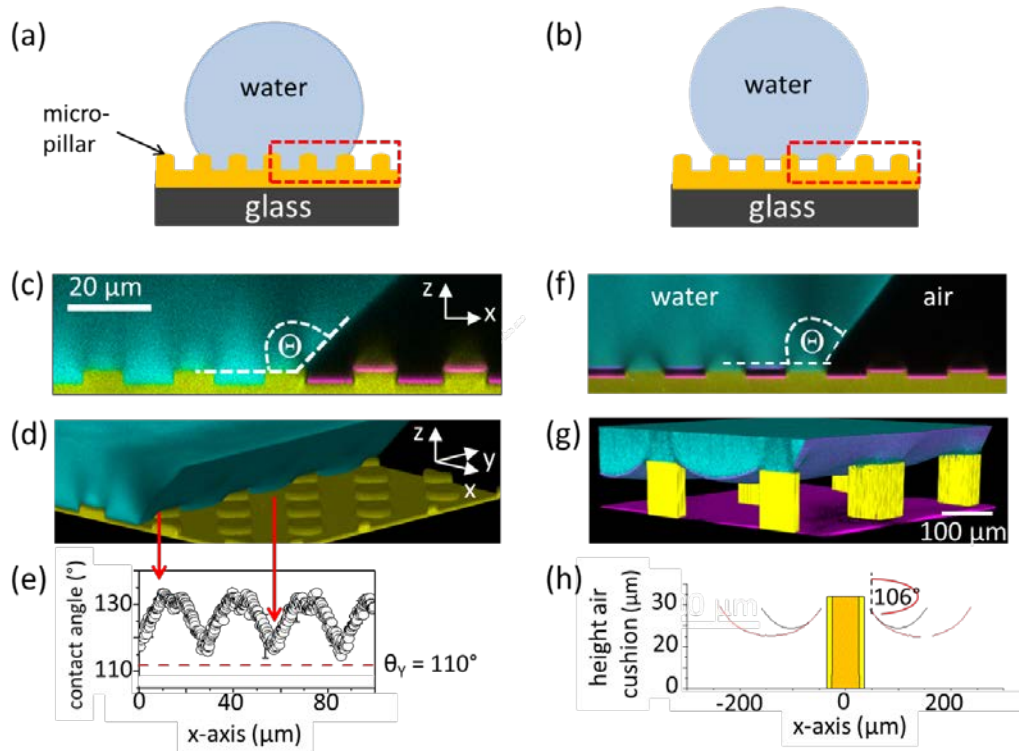


Figure 1.3 a) Sketch of a drop in the Wenzel state and (b) in the Cassie state. To image the water-substrate-air interface by laser scanning confocal microscopy (LSCM), the pillars and the water droplet were fluorescently labelled. The hydrophobic perylene monoimide (PMI, emission maximum at $\lambda_{PMI} = 540 \text{ nm}$) dye was added to PDMS or SU8 during soft-moulding. For water, perylenediimide tetrapyrroxy, WS-PDI, was used as it hardly changed the water-air interfacial tension, with $\gamma > 71 \text{ mN/m}$ at a concentration of $0.1 \text{ mg/ml} \approx 0.06 \text{ mM}$. Its emission maximum, $\lambda_{WS-PDI} = 600 \text{ nm}$, is well above that of PMI, so that the fluorescence from PDMS and water hardly overlap. (c) LSCM image of a vertical section of a water drop in the Wenzel state in contact with PDMS pillars and air. (d) A three dimensional LSCM image of a drop in the Wenzel state. (e) The apparent contact angle Θ varies along the three-phase contact line. (f), (g) LSCM image of a two dimensional section and three dimensional view of a water droplet in the Cassie state in contact with (f) PDMS and (g) SU8 pillars and air. The dry objective allows to accurately measure the thickness of the air layer, but the much higher index of refraction n of SU8, $n_{SU8} = 1.6$ causes the SU8 pillars to appear shorter by a factor of about 1.6. Therefore, artificial pillars with the actual height are inserted. (h) Variation of the thickness of the air cushion along the main axis (black) and diagonal (red). Water (blue), PDMS or SU8 (yellow) and light reflected at the PDMS-air interface (magenta). (c), (d), (f) The round PDMS pillars had the following dimensions: $a = 10 \text{ }\mu\text{m}$, $h = 5 \text{ }\mu\text{m}$, and $d = 20 \text{ }\mu\text{m}$ or $d = 40 \text{ }\mu\text{m}$. g) The square SU8 pillars had the following dimensions: $a = 50 \text{ }\mu\text{m}$, $h = 25 \text{ }\mu\text{m}$, and $d = 200 \text{ }\mu\text{m}$. Adapted with permission from Papadopoulos, P., et al., Wetting on the microscale: shape of a liquid drop on a microstructured surface at different length scales.

Langmuir, 2012. 28: p. 8392-8398. Copyright 2012 American Chemical Society. Adapted with permission from Papadopoulos, P., et al., How superhydrophobicity breaks down. PNAS, 2013. 110(9): p. 3254–3258.

In the Cassie state the drop rests partially on air cushions and partially on the pillar's top face. The air cushion gives rise to the two well separated horizontal reflections resulting from the PDMS-air (or SU8-air) and air-water interface. (Figure 1.3f) At the rim of the drop the water-air interface bends upwards. The absence of reflection on top of the pillars, supported by the fluorescence images of water and PDMS (or SU8), proved that the pillars were completely wetted by water. The water-air interface curvature of the drop is governed by the Laplace equation ($P = 2\gamma_L/R$), which relates the pressure, P , inside the drop of radius R to its curvature, $1/R$. Flattening of the drop by gravity can be neglected for drops much smaller than the capillary length, $(\gamma_L/\rho g)^{1/2} = 2.7 \text{ mm}$, where ρ is the density of water, $\gamma_L = 72 \text{ mN/m}$, and $g = 9.81 \text{ m/s}^2$. The three-phase contact line is pinned at the edge of the pillars. As the curvature of the water-air interface is determined by the Laplace pressure, the minimal thickness of the air cushion decreases with increasing pillars' spacing. The variation of the thickness of the air cushion along the main axis (black) and diagonal (red) for the drop shown in Figure 1.3g is given in Figure 1.3h.

1.1.3 Superhydrophobicity

Often the term Cassie state is used as a synonym for superhydrophobicity. However, a surface is defined as superhydrophobic if the apparent contact angle with water is above 150° and the roll-off angle is below 10° . Tilting a superhydrophobic surface by a few degrees is already sufficient for a drop to overcome adhesion, to roll off easily and wash away dirt particles encountered on its way (Figure 1.4). A drop in a Cassie state can have lower apparent contact angles and higher roll-off angles¹⁰. Therefore, the Cassie state is not necessarily superhydrophobic.

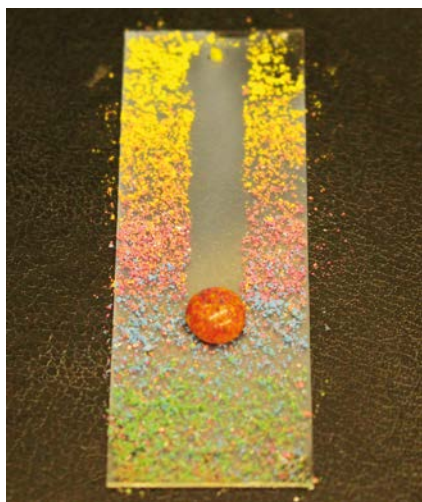


Figure 1.4 A water drop rolling-off a polluted superhydrophobic surface. The drop takes the dust along.

This extreme water repellency was first observed in nature¹¹ and can be found on insect wings¹² and legs¹³ (Figure 1.5a), many plant leaves¹⁴ like the lotus leaf¹⁵ (Figure 1.5b). These surfaces possess a multiscale (hierarchical) surface structure in combination with a low surface tension material. The surface of a water strider leg, for example, consists of numerous needle-shaped setae (Figure 1.5c) with nanoscale grooves (Figure 1.5c, inset) that enable the water strider to stand and move on water¹³. The lotus leaf surface consists of micrometer-sized papillae covered with a layer of wax crystals (Figure 1.5d, inset)¹⁶.

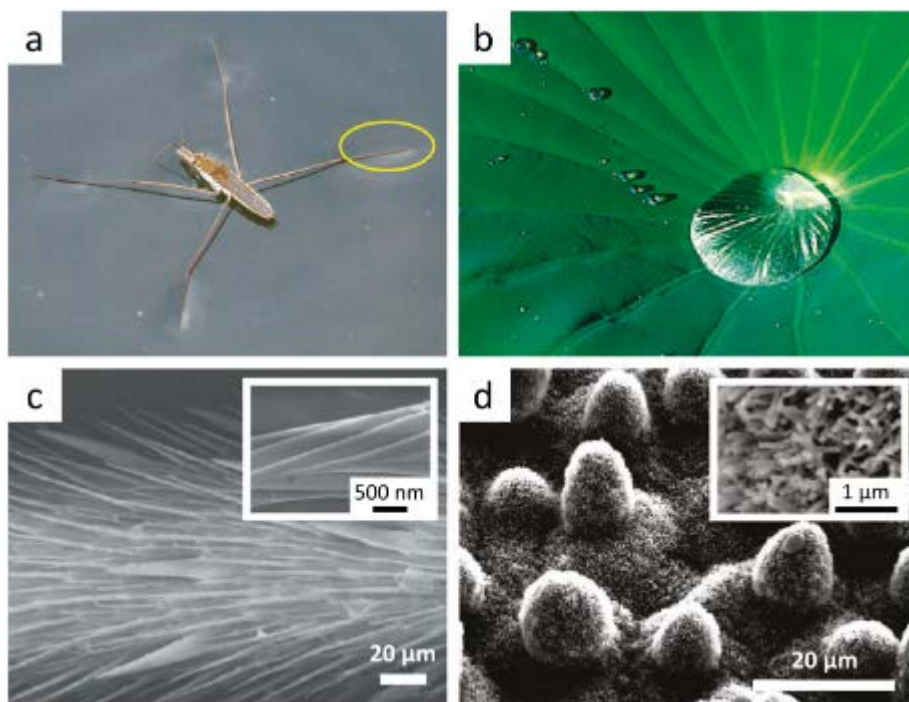


Figure 1.5 Examples for natural superhydrophobic surfaces, like the water strider leg (a) and the lotus leaf (b). Both surfaces possess a hierarchical structure on two length scales. The water strider leg surface consists of micrometer-sized setae (c) with nano grooves (c, inset) and the lotus leaf surface of micro bumps (d) covered with nanometer-sized wax crystals (d, inset). Reprinted with permission from Su, Y.W., et al., Nature's Design of Hierarchical Superhydrophobic Surfaces of a Water Strider for Low Adhesion and Low-Energy Dissipation. *Langmuir*, 2010. 26(24): p. 18926-18937. Copyright 2010 American Chemical Society.

If the superhydrophobic state should be thermodynamically stable a material with low surface free energy is required ($\gamma_s < \gamma_{sl}$), as roughness amplifies the wetting properties. According to Young's equation it was expected that superhydrophobicity requires a material contact angle above 90°. For example, poly(tetrafluoroethylene) with a surface free energy $\gamma_s = 0.0185\text{N/m}$ has a Young

contact angle with water of about 108° ¹⁷. However, superhydrophobic properties can also be observed on intrinsically hydrophilic materials^{18, 19}. This was predicted by Herminghaus theoretically²⁰. Notable, even the wax of the lotus leaf is weakly hydrophilic with a material contact angle ϑ of $\sim 74^\circ$ ²¹. Cao et al. fabricated superhydrophobic surfaces with multiscale roughness by packing hydrophilic flower-like hematite particles (Figure 1.6a). The 1-2 μm -sized $\alpha\text{-Fe}_2\text{O}_3$ particles possess a rough surface consisting of 40-60 nm thick distorted plates of interconnected crystals which remind to the petals of a flower. These distorted plates present an overhanging structure, which prevents the water from penetrating the textures. Due to the overhangs the multilayer of $\alpha\text{-Fe}_2\text{O}_3$ particles is superhydrophobic (Figure 1.6b) despite a material contact angle of $\vartheta = 45^\circ$ for $\alpha\text{-Fe}_2\text{O}_3$. The overhangs act as an energy barrier preventing a transition from the Cassie to the fully wetted state.

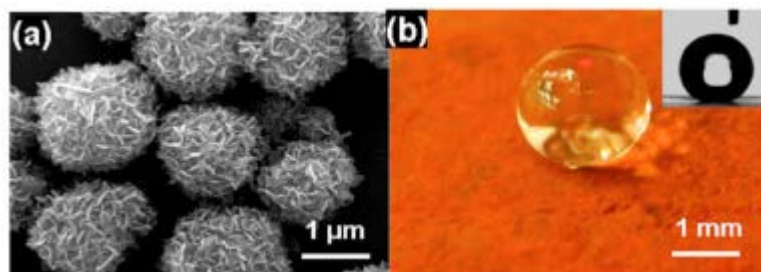


Figure 1.6 Superhydrophobic surface made of intrinsically hydrophilic hematite flower-like particles (a) showing an apparent contact angle with water of $\Theta = 159^\circ$ (b). Reprinted with permission from Cao, A.M., L.L. Cao, and D. Gao, Fabrication of nonaging superhydrophobic surfaces by packing flowerlike hematite particles. *Applied Physics Letters*, 2007. **91**(3). Copyright 2007, AIP Publishing LLC.

1.1.4 Superamphiphobicity

Whereas innumerable plants and many insects are known for their superhydrophobicity, extremely oil and water repellent, in nature so-called superamphiphobic surfaces are rare. Superamphiphobic surfaces show high apparent contact angles ($\Theta \geq 150^\circ$) in conjunction with low roll-off angles ($\alpha \leq 5^\circ$ to 10°) with water and non-polar liquids.^{22, 23} To achieve an intrinsic contact angle higher than 90° for most alkanes with a surface tension $\gamma_L = 20\text{-}30 \text{ mN/m}$ the solid surface tension γ_S should be below $\sim 6 \text{ mN/m}$.²⁴ Furthermore γ_{SL} needs to be lower than γ_S ; this has not been achieved yet. However, metastable superamphiphobicity can be induced to intrinsically oleophilic materials by creating local overhanging structures, acting as an energy barrier for the drop to impale into the coating^{23, 25, 26}. Highly advanced design of the surface protrusions even permits fluorinated solvents to rest on hydrophilic nail-like silicon pillars with vertical overhangs in a Cassie state²⁷. One example of an insect with superamphiphobic skin are the springtails which are mainly soil-dwelling wingless arthropods (Figure 1.7a)²⁸. On

their skin they can form a stable air layer, a so-called plastron. Upon immersion in water (Figure 1.7b) or oils (Figure 1.7c) the plastron protects the skin breathing animals against suffocation.

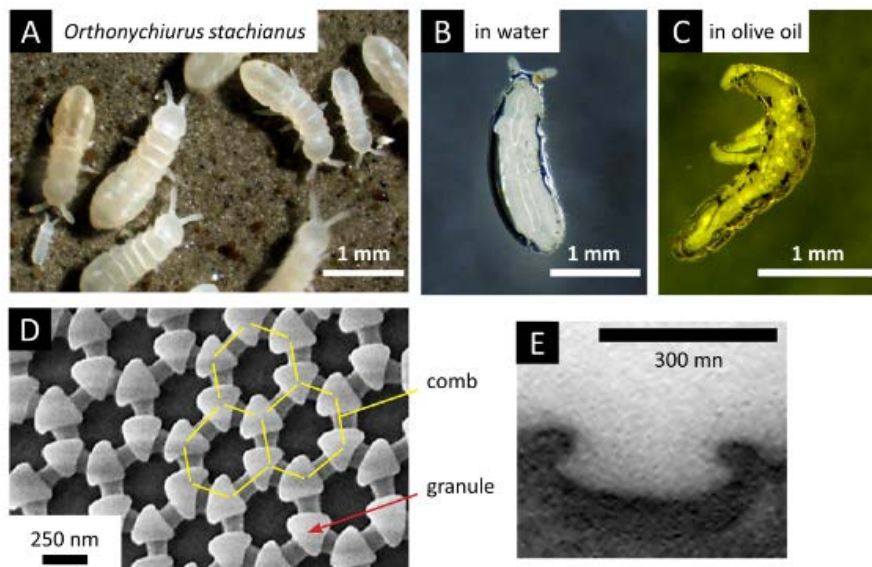


Figure 1.7 (a) Springtail colony of *Orthonychiurus stachianus*. (b), (c) Plastron surrounding the entire animal upon immersion into (b) water and (c) olive oil. (d) Scanning electron microscopy image and (e) cross-sectional transmission electron microscopy image of the nanoscopic skin ornamentation. Adapted with permission from Hensel, R., et al., Wetting Resistance at Its Topographical Limit The Benefit of Mushroom and Serif T Structures. *Langmuir*, 2013. 29(4): p. 1100-1112. Copyright 2013 American Chemical Society.

Scanning electron microscopy revealed the skin of springtails to be covered by a nanoscopic comb structure with hexagonally arranged cavities (Figure 1.7d)²⁸. Granules are located at the intersections of the combs. A cross-sectional profile of the skin, taken by transmission electron microscopy, illustrates that the cavities possess pronounced overhangs at their top edges (Figure 1.7e) similar to the petals of the flower-like particles.

Overhangs are required as on a submicrometer length scale the molecules of the drop want to minimize the interfacial energies. This results in a material contact angle below 90° for hydrophobic or non-polar liquids. As sketched in Figure 1.8, the contact line of a water drop is pinned at the upper side of a sphere (Figure 1.8a). Contrary, the material's contact angle for an oil drop is below 90°. Therefore, an oil drop is pinned at the underside of a sphere. With decreasing material's contact angle the position where the contact line is pinned moves towards the bottom of the sphere (Figure 1.8b). To prevent that the drop touches the underlying sphere, the neck connecting both spheres should be narrow.

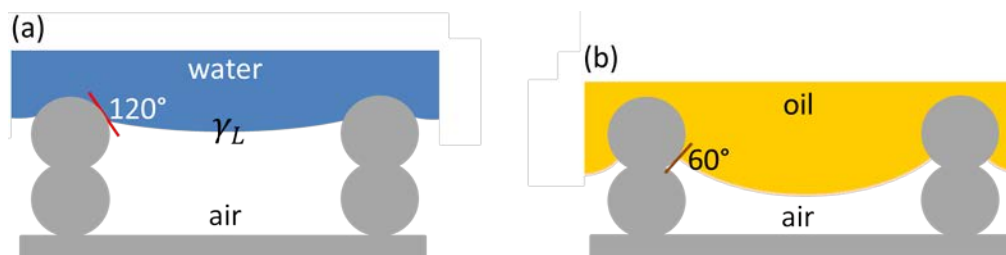


Figure 1.8 Sketch of a water drop deposited on a hydrophobic sphere. (a) The water drop rests at the top part of the sphere, to locally take its material's contact angle (here 120°). (b) The oil drop is pinned at the lower side of the sphere, as its material's contact is below 90° (here 60°). The oil drop is in a metastable state.

1.1.5 Fabrication of superamphiphobic surfaces

There are numerous techniques to construct superhydrophobic surfaces with hierarchical structures employing various materials and substrates²⁹. The fabrication of superamphiphobic surfaces is more demanding due to the complex overhang structures required. The first superamphiphobic model surface has been prepared in 2007, making use of lithography²³. Different groups picked up the strategy and fabricated superamphiphobic structures consisting of regular arrays of inverse trapezes or nail-like morphologies^{9, 30-33}. Strategies include spontaneous bottom-up^{26, 34} like spray casting³⁵, lithographic top-down^{23, 36} or combined approaches^{24, 37}. The bottom-up approach is usually simpler, cheaper and reaches smaller sub-100 nm features³⁸. Also, superamphiphobic surfaces formed by fibrous structures have been developed^{39, 40}.

In 1997, Kaoru Tsujii *et al.* successfully fabricated a surface that showed an apparent contact angle of $\Theta = 151^\circ$ for oil droplet. They modified the surface morphology of an aluminium plate by anodic oxidation (Figure 1.9). Subsequently they grafted a fluorinated monoalkylphosphates to lower the surface energy⁴¹. The surface repels liquids which have a surface tension above 40 mN/m.

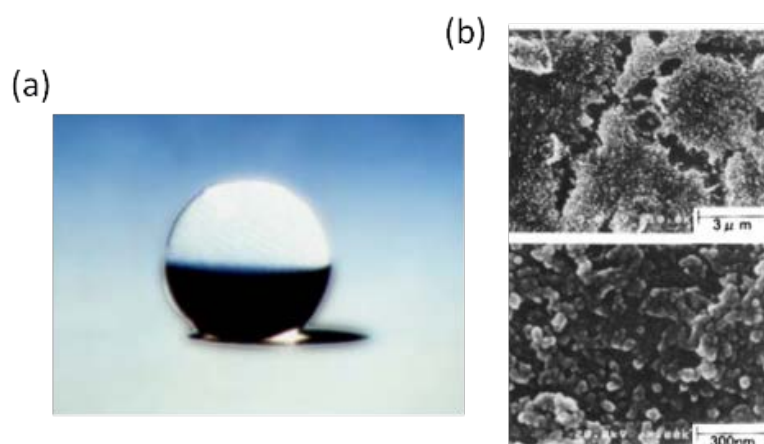


Figure 1.9 (a) A rapeseed oil droplet on a superamphiphobic surface. (b) SEM images of the surface taken at two different magnifications, showing an anodically

oxidized aluminum plate surface. Tsujii, K., et al., Super Oil-Repellent Surfaces. *Angewandte Chemie International Edition in English*, 1997. 36(9): p. 1011-1012. Copyright Wiley-VCH Verlag GmbH & Co. KGaA. Reproduced with permission.

Tuteja *et al.* fabricated a superamphiphobic surface composed of so called „micro-hoodoos” (Figure 1.10a). This model surface rendered it possible to calculate the impalement pressure in dependence of the size and spacing of the micro-hoodoos. The impalement pressure is the pressure that needs to be overcome that a drop passes the transition from the Cassie to the Wenzel state. Furthermore, Tuteja *et al.* fabricated superamphiphobic meshes and showed their performance to separate water and oil. Therefore, they synthesized polyhedral oligomeric silsesquioxane (POSS) in which the rigid silsesquioxane cage was surrounded by perfluoro-alkyl groups. The surface energy of the matrix can be systematically changed by varying the mass fraction of fluoroPOSS molecules blend with PMMA (Figure 1.10b). After electrospinning, the fluoroPOSS molecular form a fibre structure.

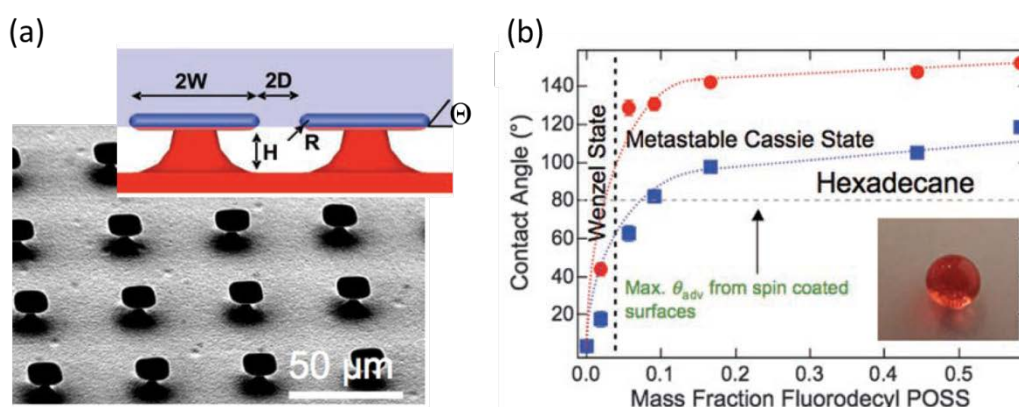


Figure 1.10 (a) Superamphiphobic surface prepared by lithography. Scanning electron microscopy images of a surface coated with “micro-nails” having flat caps. Inset: Cartoon highlighting the formation of the composite interface with overhang structures. (b) Advancing apparent contact angle and receding apparent contact angle for hexadecane, respectively, on the electrospun surfaces. The inset shows a drop of hexadecane (dyed with Oil Red O) on a 44 weight % fluorodecyl POSS electrospun surface. From Tuteja, A., et al., Designing superoleophobic surfaces. *Science*, 2007. 318(5856): p. 1618-1622. Reprinted with permission from AAAS.

A simple and highly oil repellent strategy is based on templating soot (Figure 1.11)²⁶. First, a several $10\ \mu\text{m}$ layer of candle soot is deposited on a substrate (Figure 1.11a, b). Soot consists of 30 to 50 nm sized carbon particles which form a fractal-like highly porous network. The soot particles are covered with a $20 \pm 5\ \text{nm}$ thick silica shell (Figure 1.11b, d, e). After removing the carbon interior of the particles by calcination at $600\ ^\circ\text{C}$ the layer is transparent (Figure 1.11j). Finally, the silica layer is hydrophobized by chemical vapour deposition with a semi-fluorinated silane to

reduce the surface energy. Drops of water and hexadecane show apparent contact angles of $165 \pm 1^\circ$ and $156 \pm 1^\circ$ and tilting angles of $1 \pm 1^\circ$ and $5 \pm 1^\circ$, respectively (Figure 1.11g, h) ²⁶. The drops rest in a metastable state on the top layer of the coating.

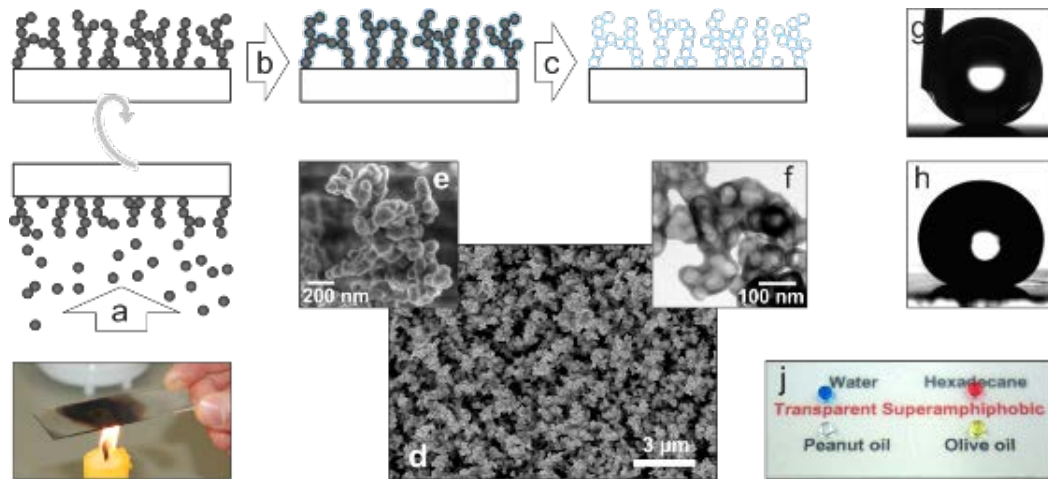


Figure 1.11 (a-c) Schematic to make superamphiphobic layers. (d-e) SEM image of the fractal-like structure of the layer before calcination. (f) TEM image of the structure after calcination. (g) Water drops form an apparent contact angle of 165° , (h) hexadecane forms an apparent contact angle of 156° . (i) Photograph of a drop of dyed water, peanut oil, olive oil, and hexadecane deposited on a superamphiphobic glass slide. The coated slide was placed on labelled paper to demonstrate transparency. Adapted from Deng, X., et al., Candle Soot as a Template for a Transparent Robust Superamphiphobic Coating. *Science*, 2012. 335(6064): p. 67-70. Reprinted with permission from AAAS.

1.1.6 Stability of the Cassie state

1.1.6.1 Stability against impalement

The stability of the superhydrophobic or superamphiphobic state is decisive for the use of the surfaces in real applications. As soon as the drop passes the transition to the Wenzel state, the surfaces loses its unique wetting properties such as self-cleaning and easy roll-off. In general the so termed Cassie-to-Wenzel transition is irreversible, in particular if the transition was caused by mechanical damage of the surface or an increase of the surface energy due to chemical decomposition or destruction of the coating by strong acids or bases. The Cassie to Wenzel transition can also be induced by applying an external pressure, evaporation of the drop, condensation of dew or a liquid in the coating ⁶. In general, the transition is accompanied by a decrease of the apparent contact angle and an increase of the roll-off angle due to increased adhesion of the drop on the surface (Figure 1.12) ⁴².

To lift a drop from the Wenzel to the superhydrophobic Cassie state external energy is required to overcome the energy barrier ⁴³. A reversible switching

between a wetted Wenzel and a superhydrophobic Cassie state could be realized by the application of electrical voltage and current (Figure 1.12)⁴⁴. A Pt wire was dipped into a water drop deposited on a superhydrophobic nanostructured surface (Figure 1.12a) that was in direct contact with a conductive substrate. Application of a potential difference between the water and the underlying substrate caused the Cassie-to- Wenzel transition (Figure 1.12b). After removal of the voltage the drop remained in the wetted state. To reverse the Cassie-to-Wenzel transition a short pulse of electrical current was transmitted through the substrate, causing a momentary increase of the surface temperature and the formation of a thin vapour layer which levitates the droplet back into the Cassie state (Figure 1.12c).

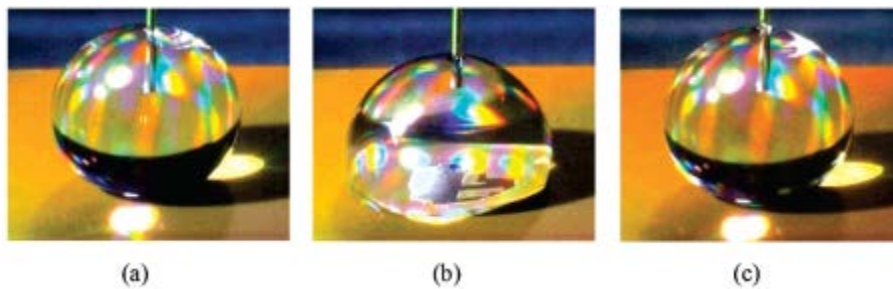


Figure 1.12 Electrically induced reversible transitions between different wetting states of a water drop on a nanostructured substrate (a-c). Adapted with permission from Krupenkin, T.N., et al., Reversible wetting-dewetting transitions on electrically tunable superhydrophobic nanostructured surfaces. *Langmuir*, 2007. 23(18): p. 9128-9133. Copyright (2007) American Chemical Society.

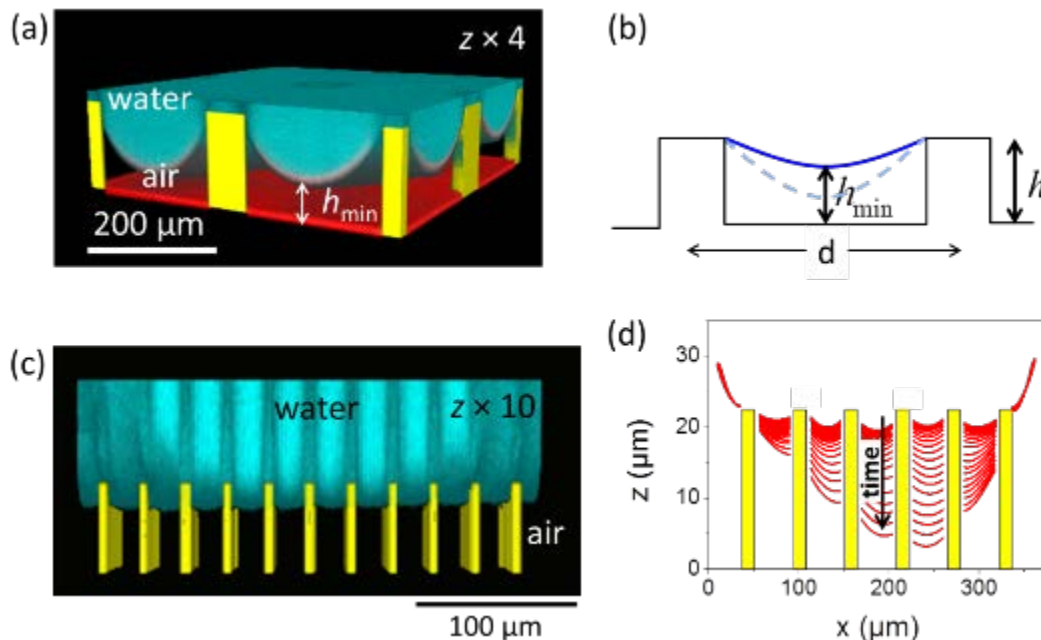


Figure 1.13 (a) LSCM images of the sagging mechanism of the Cassie-to-Wenzel transition. The array dimensions are $a = 50 \mu\text{m}$, $h = 23 \mu\text{m}$, $d = 200 \mu\text{m}$. For better visualization, the z-axis is 4 times magnified. (b) Variation of the thickness of the air

cushion. h_{min} denotes the minimum thickness. (c) LSCM images of the depinning mechanism of the Cassie-to-Wenzel transition. Complete contact area view of a drop during the Cassie-to-Wenzel transition on an array with $a = 5 \mu\text{m}$, $h = 5 \mu\text{m}$, $d = 20 \mu\text{m}$. The z-axis is 10× magnified. (d) Dependence of the thickness of the air cushion along a diagonal passing through the centre of the drop. The red lines are fits to the drop profile. Profiles are taken at 3s apart. The array dimensions are $a = 10 \mu\text{m}$, $h = 23 \mu\text{m}$, $d = 40 \mu\text{m}$. Adapted with permission from Papadopoulos, P., et al., How superhydrophobicity breaks down. PNAS, 2013. 110(9): p. 3254–3258.

The Cassie to Wenzel transition typically passes via the sag (Fig. 1.13a) or the depinning (Fig. 1.13c) mechanism⁴⁵⁻⁴⁷ as illustrated by LSCM images. The transition was induced by an increase of the Laplace pressure as the water drop evaporated. The impalement of the drop into the layer can be monitored by recording the thickness of the air cushion (Figure 1.13b). In the sag-mechanism the rim of the drop remained pinned at the top face of the pillars. The curvature of the water-air interface gradually increases while the drop evaporates (Figure 1.13b). The drop passes the transition to the Wenzel state as soon as the lowest point of the meniscus touches the bottom surface. The minimum thickness of the air cushion can be calculated if the maximum spacing of neighbouring protrusions and the radius of the drop, R , is known. In case of a micropillar array arranged on a square lattice the largest value of the mean curvature is obtained at the centre of the diagonal connecting neighbouring pillars. The thickness of the air cushion, h_{min} , follows from geometrical considerations and decreases with increasing pillar-pillar distance and decreasing radius of the water drop.

$$h_{min} = h - \left(R + \sqrt{R^2 - 0.5d^2} \right) \quad (5)$$

The liquid interface touches the bottom of the substrate for $h_{min} = 0$. The corresponding maximum Laplace pressure is given by³⁸:

$$P = \frac{2\gamma}{R} = \frac{8\gamma h}{d^2 + 2h^2} \quad (6)$$

It is important to keep in mind that the largest spacing between and the lowest height of the pillars determines the stability of the Cassie state. Mechanical damage of the surface can locally increase the spacing between neighbouring protrusions, causing that the drop touches its base. Sagging forms a problem for the design of transparent superhydrophobic surfaces. To reduce haze, the superamphiphobic layer should be as thin as possible, preferentially below half a micrometre. In that case, a few micrometres wide spacing between neighbouring protrusions can already be sufficient that the drop touches the base.

In the depinning mechanism the three phase contact line unpins from the edge of the protrusions and slides down its wall (Figure 1.13c,d). Depinning starts if the contact angle exceeds the advancing contact angle of the corresponding flat surface of identical material, measured from the vertical⁴⁸. In reality, depinning does not proceed simultaneously from all pillars but depends on small differences of the smoothness and chemical composition of the pillar's edge (Figure 1.13d).

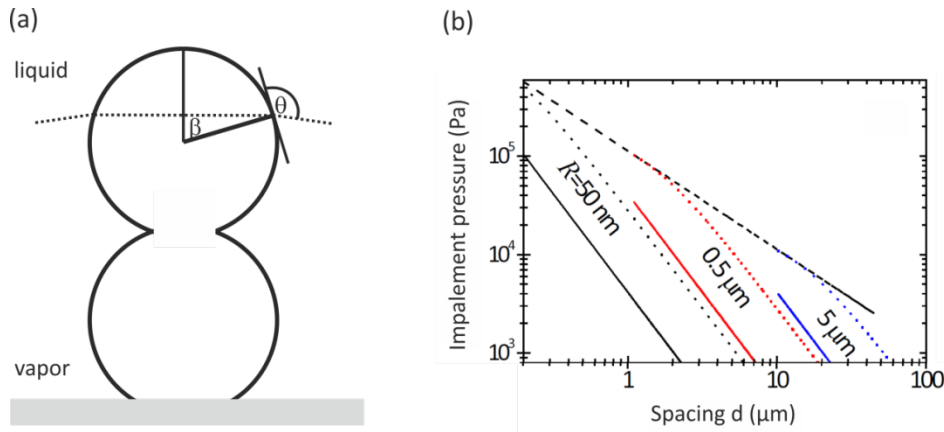


Figure 1.14 (a) Sketch of a drop on a hydrophobic sphere. (b) Impalement pressure for a liquid deposited on an array of spheres arranged in columns for different size and spacing between neighbouring columns. Adapted from Butt, H.J., et al., Design principles for superamphiphobic surfaces. *Soft Matter*, 2013. 9(2): p. 418-428 with permission from The Royal Society of Chemistry.

The pressure to induce depinning depends on the shape of the protrusions. For simplicity, we assume spherical protrusion. A water drop on a hydrophobic surface has a material contact angle above 90° . Therefore, a water drop is pinned at the upper side of the sphere. Deviations from the material contact angle are energetically unfavourable, i.e. the drop needs to overcome an energy barrier. In case of large spacing between the spheres, the maximum capillary force is given by:

$$F_c = 2\pi\gamma R \sin\beta \sin(\theta_A - \beta) \quad (7)$$

β is the angle describing the position of the three phase contact line on the particle surface (Figure 1.14a).

$$F_c = 2\pi\gamma R \sin^2(\theta_A/2) \quad (8)$$

The maximal capillary force per protrusion can be exceeded by applying an external pressure. The critical pressure, the so termed impalement pressure, is given by the maximum capillary force per area covered by one pillar, $P = F_c/A$. If the spheres (or columns of spheres) are arranged on a square lattice ($A = d^2$), P is given by³⁸:

$$P = 2\pi\gamma R/d^2 \sin^2(\theta_A/2) \quad (9)$$

The impalement pressure decreases with increasing lattice spacing or large sphere size (Figure 1.14b). b). This derivation assumes that the necks, connecting neighbouring spheres is small, i.e. the material advancing contact angle should not be affected by the sphere underneath. For a monolayer of spheres and low ϑ_A the drop may touch the top side of the sphere underneath or the base before depinning occurs.

The impalement pressure does not depend on the hydrophilicity of the sphere's topmost part. In case of micropillar arrays this implies that the pillar's top face can be hydrophilic¹⁰. Essential is that the side walls are hydrophobic to ensure a large advancing contact angle. However, hydrophilic top faces reduce the apparent receding contact angle, resulting in an increase of hysteresis. The apparent receding contact angle follows from balancing the forces at the rim of a drop³⁸.

$$\Theta_r = \pi \left(1 - \frac{2R}{d} \cos^2 \frac{\theta_R}{2} \right) \quad (10)$$

For a given material receding contact angle ϑ_A , the apparent receding contact angle only depends on the ratio d/R which should be as high as possible to achieve a high Θ_r . A decreasing apparent receding contact angle increases the solid-liquid adhesion force as:

$$F_{LA} = \gamma b k (\cos \Theta_r - \cos \Theta_a) \quad (11)$$

Here, b is the effective width of the drop in contact with the solid. $k \approx 1.5$ is a constant which varies slightly depending on the specific shape of the contact area⁴⁹. Therefore, surfaces with low Θ_r are rarely superhydrophobic or superamphiphobic. However, the drop still can be in the Cassie state.

1.1.6.2 Mechanical stability

The mechanical stability of super liquid repellent layers is essential for many real-life applications. The longevity of super liquid-repellent surfaces can be increased by two main approaches which are ideally combined.

The first approach focuses on reducing the consequences of surface damage and the second approach considers how to restore surface roughness/chemistry after damage^{50, 51}. The consequences of surface damage can be reduced by the combination of micro- and nanorough structures⁵²⁻⁵⁴. Ideally, the nanoroughness should provide good liquid repellency and the microrough structures should ensure good mechanical stability (Figure 1.15a). Given that the damage only partially

destroys the microroughness, the sheltered regions keep their nanoroughness. If this is true liquid drops can still rest on nanoprotusions and easily roll-off.

Often hydrophilic templates are used which are post-treated with a hydrophobic coating. Surface damage will cause the hydrophilic bulk material to be revealed (Figure 1.15b, bottom). These hydrophilic spots lead to an increase of the receding contact angle and therefore to an increase of solid liquid adhesion. Therefore, another approach emphasizes the role of the bulk material used to prepare the super-liquid repellent surface. Upon surface damage bulk material can be exposed to the liquid. A motivation to use hydrophobic bulk materials is that the newly created interface will also be low in energy. Ideally, the surface chemistry is the same before and after the damage (Figure 1.15b, top).

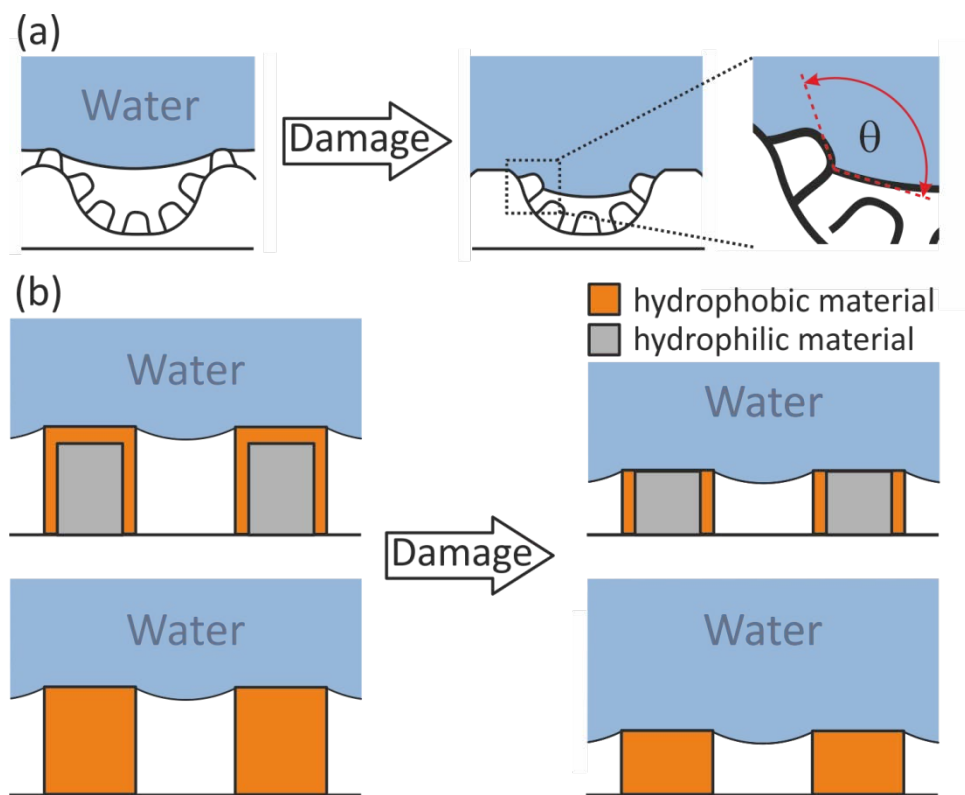


Figure 1.15 (a) A micro and nanorough surface is exposed to surface damage. The microroughness provides shelter for the nanorough structures, which is required for a stable Cassie-Baxter state. Magnification: The three-phase contact line is efficiently suspended on the nanorough structure details under local fulfilment of the material contact angle θ . (b, top) Damage of a hydrophobic coating can reveal hydrophilic bulk material (grey). The Cassie state can still be stable though drop adhesion is increased. (b, bottom) Damage of hydrophobic (orange) material will expose new interface with same surface chemistry, ideally not changing repellency.

Several methods have been applied to quantify mechanical stability. Assessing “how stable” layers are, is however not trivial. Depending on the materials used, the layer thickness, the specific shape of the surface protrusions and the overall

porosity, large differences in the mechanical stability of super liquid-repellent layers can be obtained. This strongly complicates the adoption of standard testing routines and so far no universal protocol exists. Accordingly, numerous protocols for testing of mechanical properties can be found in the literature, e.g. reviewed in ⁵⁵. The protocols differ in how and how much load/wear was applied to the surface and how the analysis of the experiment is conducted. For simplification, we suggest classification of tests in two categories:

Category 1: Load/wear is applied to a macroscopic area (at least a few mm). Examples are tape test ^{56, 57}, wiping of tissues ⁵⁸, sand impact ⁵⁷ or laundry cycles ⁵⁹. After the test, the sample are analysed by image based techniques, e.g. by optical or electron microscopy. Importantly, the apparent contact angles before and after surface treatments are measured. The advantage of this category is its good accessibility and simple analysis. Nevertheless, macroscopic tests are likely to fail resolving the difference of layers having similar mechanical properties.

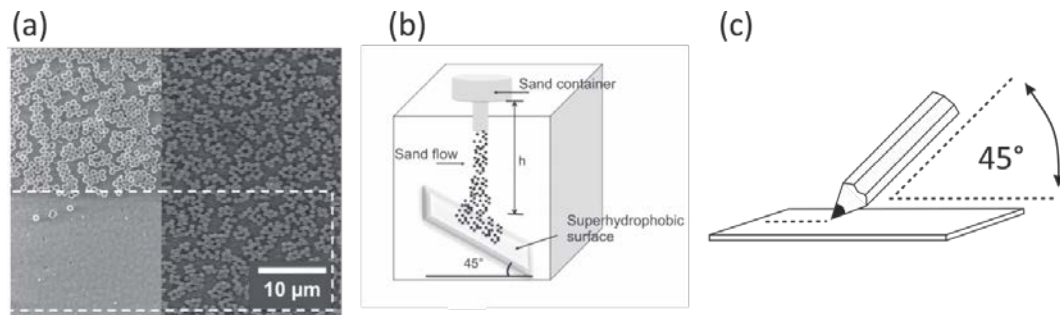


Figure 1.16 (a) A superhydrophobic surfaces made of hollow silica particles was partially exposed to double sided tape (white boxes indicate the exposed areas). (a, left) The particles only adhere by van der Waals force to the substrate and are easily removed by the tape test. (a, right) Particles are chemically fixed by chemical vapor deposition of silica. The particles were not removed from the substrate by the tape test. (b) Schematic setup to determine surface stability against impact of sand grains. The kinetic energy of the sand grains can be varied by changing the distance h between surface and container. (c) Scheme of the pencil hardness test. Pencils with different hardness (9H(hard) – 9B(soft)) are pushed/pulled over a surface at an angle of typically 45°. The resistance of the coating is given by the hardest pencil unable to scratch the surface. Adapted from “Transparent, Thermally Stable and Mechanically Robust Superhydrophobic Surfaces Made from Porous Silica Capsules”. Deng, X., et al. *Advanced Materials*, 23(26): p. 2962-+. Copyright (c) 2011.

Category 2: Load/wear is applied to a microscopic area (several hundred μm too few nm). In this case, the affected area is too small for reasonable contact angles measurements before and after surface damage. One popular example is the pencil hardness test where pencils of different hardnesses are drawn over a surface until one pencil type fails to scratch the surface ⁵⁶. For some tests the International

Organization of Standardization (ISO) and the American Society for Testing and Materials (ASTM) defined specific guidelines. Still these tests have their limitations and the comparability of the results might be hindered by the tape model, pressing load and pencil model⁵⁵. Nanoindentation or atomic force microscopy (AFM) based approaches are more sensitive and quantitative. By combining nanoindentation and AFM a force range between a few nano-Newton to several milli-Newton can be covered. Both techniques are highly sensitive⁶⁰. Nanoindentation and atomic force spectroscopy also gives the Young's modulus E and the hardness H ^{58, 61-63}. This can provide precious information for optimization of individual system. It also bears the potential to simplify comparison of surfaces between different groups. -However, the measurements themselves can be challenging as the penetration depth should be smaller than 10% of the film thickness to neglect substrate effects. For individual super liquid-repellent layers this might cause a problem due to their poor mechanical stability or small film thickness or both. Visualization of the indentation area, often required for the elastic modulus and the hardness in nanoindentation, can be cumbersome for very porous surfaces. Last but not least due to the high surface roughness, the size ratio of the indenter to the surface features needs to be considered and taken care off for the interpretation of the results. Improving and characterizing the mechanical stability of super liquid-repellent is and will remain one of the most challenging aspects towards their broad appliance in everyday life.

1.2 Potential Applications

Prospective applications of superhydrophobic and superamphiphobic surfaces range from self-cleaning^{14, 64, 65}, drug reduction⁶⁶⁻⁶⁸, anti-biofouling^{69, 70}, sensors⁷¹⁻⁷³, liquid repellent textiles⁷⁴⁻⁷⁶, gas contactor membranes⁷⁷, to surfaces for particle synthesis⁷⁸⁻⁸⁰.

1.2.1 Polymeric Particles in the mm to μm Range

Polymeric particles grew more and more important over the last decades and became an important part of everyday life, e.g. in coatings, cosmetics and electronics^{81, 82}. Common polymerization techniques are e.g. suspension, dispersion, emulsion and miniemulsion polymerization or microfluidics^{83, 84}. All methods have in common, that particles are produced, functionalized and processed in solvents. The solvents are essential for heat transfer and to control the particle shape. Typically, minimization of free energy dictates a spherical shape of the initial monomer drops or growing particle and this geometry is maintained in the final product.

Superhydrophobic surfaces were used to prepare particles by solvent evaporation^{79, 80, 85, 86}. An aqueous dispersion was deposited on a superhydrophobic surface. After evaporation of water particles the dispersed nanoparticles formed spherical aggregates. The shape of the particles can be tuned by adjusting the concentration

of the dispersion and the properties of the superhydrophobic or superamphiphobic surface.

Superamphiphobic surfaces renders further strategies possible as superamphiphobic surfaces are repellent towards many organic low surface tension liquids, including several monomers and functional liquids (Figure 1.17). Particles can be fabricated via physical (tuning temperature⁷⁸, solvent evaporation^{79, 85}) or chemical polymerization⁷⁸ strategies. Compared to classical polymerization techniques, particle synthesis on superamphiphobic surfaces neither requires solvents nor additives.

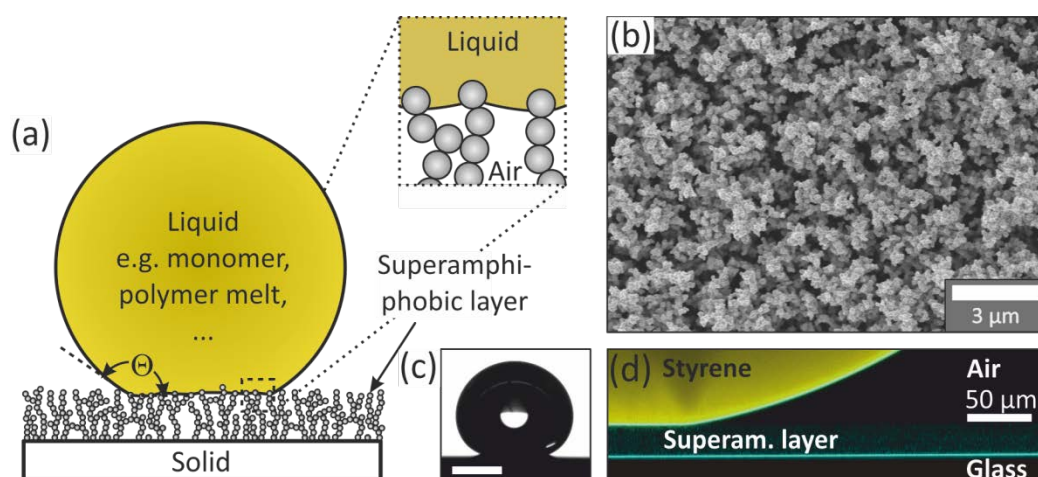


Figure 1.17 Liquid drop on a superamphiphobic layer. (a) Schematic of a liquid drop on a superamphiphobic layer and a magnified view of the interface between the liquid and the superamphiphobic layer. (b) Scanning electron microscope (SEM) image of a superamphiphobic layer. (c) Video image and (d) vertical section through a drop of styrene on a superamphiphobic layer imaged with a confocal microscope. Scale bar in c is 1 mm. The 6 μL drop was labeled with 0.04 mg/mL N-(2,6-diisopropylphenyl)perylene-3,4-dicarbonacidimide. It appears yellow. The original excitation light in blue caused by reflection at interfaces shows the top surface of the glass and the bottom surface of the styrene drop. In between, with some weak scattering at the silicon oxide nanostructures the superamphiphobic layer can be seen. Adapted from “Solvent-Free Synthesis of Microparticles on Superamphiphobic Surfaces”. Deng et. al. *Angewandte Chemie-International Edition*, 52(43): p. 11286-11289. Copyright (c) 2013.

1.2.2 Particle synthesis via tuning temperature

This strategy makes use of the temperature dependence of the physical interactions of polymers. A polymer powder, a polymer blend, or a mixture a polymer powder with nanoparticles is sprinkled onto the superamphiphobic layer and heated above its glass transition temperature, T_g . (Figure 1.18a). While heating

the powder, the viscosity gradually decreased and the agglomerates start to shrink and transform to spherical microspheres (Figure 1.18b). The spherical shape is preserved after cooling the particles below T_g . The size of the final microspheres is given by the volume of the initial powder agglomerate and thus by the dispersion and size of the agglomerates. Janus microspheres can be produced by mixing two polymers, for example polystyrene and poly(methyl methacrylate (Figure 1.18b). To distinguish the two polymers, the fluorescent dye rhodamine 6G was covalently attached to the polystyrene. The dyed blend was sprinkled on the superamphiphobic surface and annealed at 160 °C. This temperature is well above the glass transition temperatures of both dyed polystyrene ($T_g = 91$ °C) and poly(methyl methacrylate ($T_g = 120$ °C). The different stages of the phase separation process were monitored by video microscopy (Figure 1.18b). After 7 minutes a microparticle with two separate domains was obtained. Finally, the structure freezes when the temperature is lowered below T_g . This approach to produce Janus particles leads to particles with well-separated surface properties.

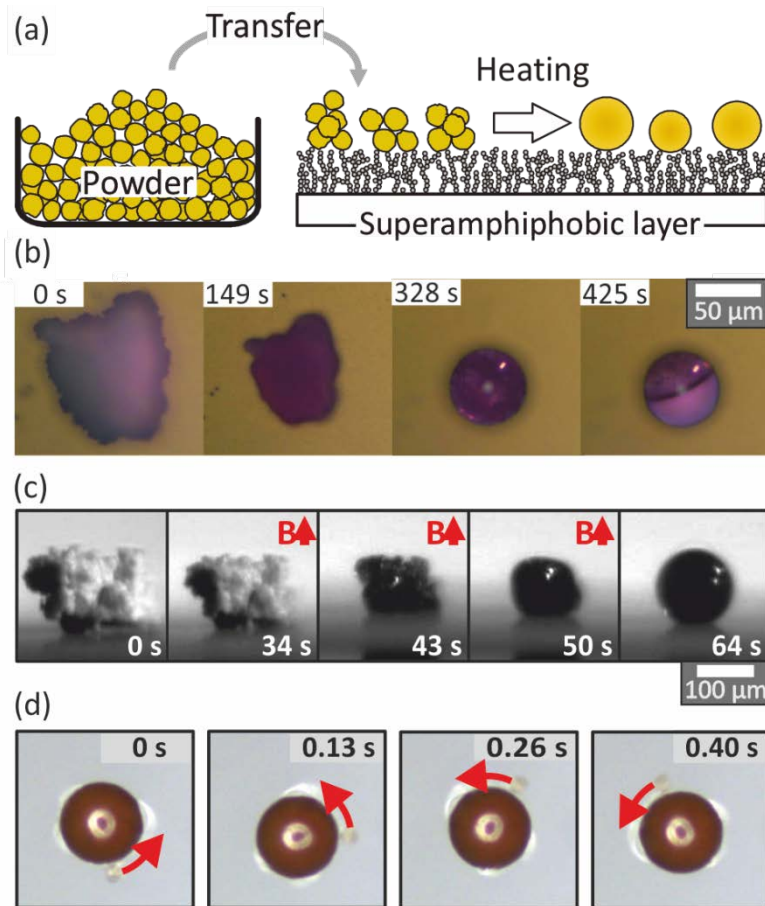


Figure 1.18 (a) Schematics of particle synthesis via tuning the temperature. A polymer powder/blend is placed on a superamphiphobic surface and annealed above T_g . (b) Sequence of video microscopy images showing annealing of an agglomerate of polystyrene dyed with rhodamine B (PS-dye, $MW = 13800$ g/mol, $T_g = 91$ °C) and poly(methyl methacrylate (PMMA, $MW=9500$ g/mol, $T_g = 120$ °C,

surface tension: $\gamma = 43$ mN/m at 120°C) for 7 minutes. The polymer blend contains PS-dye/PMMA (1:1 w/w). (c) Sequence of optical microscope images starting with an iron oxide containing agglomerate of polystyrene ($M_w = 5800$ g/mol, polydispersity, $T_g = 78$ °C, surface tension: $\gamma = 32$ mN/m at 120°C). Microspheres formed after annealing for more than 1 minute at 100°C. The polymer melt is exposed to a magnetic field during annealing for anisotropic arrangement of the iron oxide particles. (d) After cooling the magnetic microsphere are transferred to the air-water interface and exposed to a rotating magnetic field (1.3 ± 0.1 mT, 14 Hz). The magnetic microparticles rotated according to the external field. A small plastic bead was attached to the magnetic PS-particle to visualize the rotation (indicated by arrows). Adapted from “Solvent-Free Synthesis of Microparticles on Superamphiphobic Surfaces”. Deng et. al. *Angewandte Chemie-International Edition*, 52(43): p. 11286-11289. Copyright (c) 2013.

Magneto-responsive microspheres were prepared by mixing iron oxide nanoparticles with PS. The agglomerates were placed on the superamphiphobic surface and the surface was annealed at 165 °C. During annealing, a magnetic field was applied to orient the iron oxide nanoparticles (Figure 1.18c). The nanoparticles diffused through the PS matrix towards the magnet leading to an anisotropic distribution inside the microsphere. After cooling, the nanoparticles are frozen in the matrix and the composite microspheres possess a permanent magnetic dipole moment. This was demonstrated by dispersing individual microspheres in water and exposing them to a weak rotating magnetic field. The microspheres rotate in a well-controlled manner with a rotation frequency corresponding to the external magnetic field (Figure 1.18d).

1.2.3 Particle synthesis via radical polymerization

This strategy makes use of the high repellency of the superamphiphobic surface versus certain monomers as show in table 1.

Table 1: Apparent contact angle Θ , roll-off angle α , and surface tension γ of monomers on a superamphiphobic surfaces at 20°C. Adapted from “Solvent-Free Synthesis of Microparticles on Superamphiphobic Surfaces”. Deng et. al. *Angewandte Chemie-International Edition*, 52(43): p. 11286-11289. Copyright (c) 2013.

Monomer	Θ	α	γ (mN/m)
Styrene	158°	6°	34
Methyl methacrylate	156°	10°	28
Acrylic acid	154°	7°	29

Adipoyl chloride	152°	9°	38
Ethylenediamine	152°	16°	42

For demonstration, bi-functional methacrylate derivatives were radically polymerized since they have a broad application in industry and medicine. Triethylene glycol dimethacrylate (TEGDMA) and bisphenol A glycerolate dimethacrylate (Bis-GMA) mixtures for example were extensively studied as they form part of dental resins. For the convenience of the patient, these resins are cured photochemically on a short time scale (seconds to few minutes)⁸⁷.

A mixture of GMA, TEGDMA, and initiator (Phenylbis(2,4,6-trimethylbenzoyl)phosphine oxide, Irgacure 819) was prepared and a 20 µl sized drop was placed on a concave watch glass coated with a superamphiphobic layer. The polymerization was initiated by pulsed UV irradiation. The drop was moved continuously while the polymerization proceeded, (Figure 1.19a). Drop motion reduced impalement of the mixture into the top-most part of the superamphiphobic layer and allowed to suppress a flat contact area in the final particle. After 2 minutes reaction time, a sphere-like solid polymeric particle was synthesized, (Figure 1.19b) and c). However, depending on the mechanical stability of the superamphiphobic coating the top layer can be peeled off by the moving particle in the course of the polymerization. As a result, particles can partially be coated with layer material. The size of the microsphere corresponds to the initial volume of the monomer drops. Depositing the monomer mixture with a pipette, the microparticles have a diameter up to ~2.5 mm. If the monomer mixture is deposited with a nanoplotter the particle size is in the order of a few tens of a micrometer, (Figure 1.19d). There is a lower fundamental limit for the particle size which is given by the average spacing between the protrusions. If the diameter of the liquid drop is smaller than about 10 times the average protrusion distance, adhesion starts to dominate and particles adhere strongly to the surface. The average protrusion distance for candle soot based superamphiphobic layers is 1-2 µm, which means the lower limit for particle size is about 20 µm in diameter.

Despite the success of the different strategies, particle synthesis on superamphiphobic surfaces is a two-dimensional process, and techniques for high throughput still need to be established.

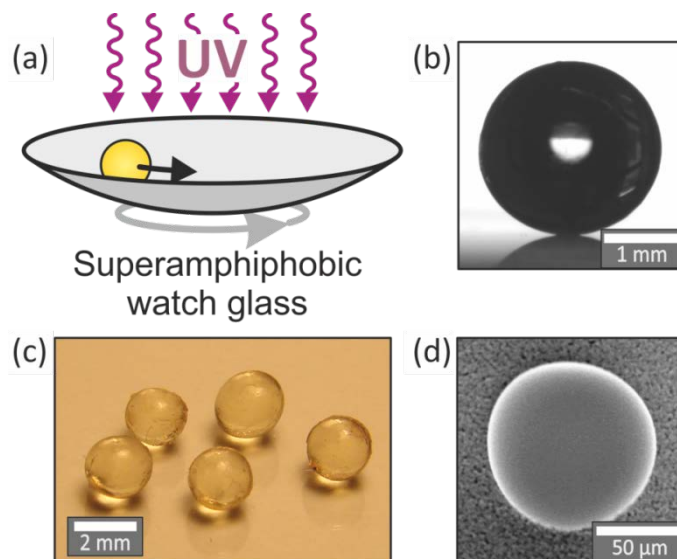


Figure 1.19 Synthesis of microspheres by radical polymerization. a) Schematic of the set-up. b, c) Particles synthesized from bis-GMA (15 wt %), TEGDMA (84 wt %), and photoinitiator (1 wt %). After mixing and sonication for 30 min, a drop (8–10 mL) was pipetted onto a concave watch glass coated with a superamphiphobic layer. The polymerization was initiated by pulsed UV irradiation for 1 min followed by continuous illumination for 4 min (LQ 400, UV-A: 200 mWcm^{-2} at the end of the glass fiber). d) SEM image of a microsphere from 99 wt % TEGDMA with 1 wt % photoinitiator polymerized by UV exposure for 3 min. The mixture was deposited by an inkjet printer (Nano-Tip AJ 070-401) held at a distance of 4 cm. Adapted from “Solvent-Free Synthesis of Microparticles on Superamphiphobic Surfaces”. Deng et. al. *Angewandte Chemie-International Edition*, 52(43): p. 11286-11289. Copyright (c) 2013.

1.2.4 Protein and Cell Adhesion on Superamphiphobic Layers

Adhesion of proteins, bacteria or cells on surfaces concerns a wide range of different domains, from food processing⁸⁸ to health care and can cause serious health risks such as inflammations⁸⁹. Once proteins, bacteria or cells found anchoring points on the surface, more and more of these will attach to the present ones and agglomerations will be formed^{90, 91}. One strategy to prevent the formation of biofilms focuses on coatings, releasing biocidal compounds, such as silver ions or antibiotics^{90, 92-94}. Another strategy is to suppress biofilm formation by designing coatings that prohibit the adsorption of cells, bacteria or proteins, for example using low-energy-surfaces (e.g. PEG or Teflon)^{95, 96} or by inducing nano-or microroughness⁹⁷⁻⁹⁹.

Lately, superhydrophobic surfaces were tested for their ability to prevent attachment of blood¹⁰⁰, platelets¹⁰¹, bacteria¹⁰², and proteins⁶⁹ under stationary or flow^{70, 101, 102} conditions. Superhydrophobic Teflon tubes (PTFE) were implanted in pigs and rabbits to investigate their anti-adhesion performance for cells

compared to classical Teflon tubes¹⁰³. Reduced^{101, 102}, enhanced¹⁰³, time¹⁰⁴ and cell type¹⁰⁵ dependent adsorption was recorded. In general, laminar flow of the liquid slows down adhesion due to a reduced dwell time for anchoring, promoted desorption, and reduced collision frequency of the material with the surface due to a finite slip length^{70, 101}.

Blood easily impales a superhydrophobic surface, resulting in an increased contact area with the substrate. The reason for impalement is the low interfacial tension of blood, $\gamma = 47 \text{ mN/m}$. Superamphiphobic coatings prevent impalement of blood into the coating. A drop of heparinized whole human blood deposited on a superamphiphobic surface showed high contact angle values of $162 \pm 1^\circ$ and low tilting angles of $5 \pm 1^\circ$ (Figure 1.20a). A sharp boundary between the superamphiphobic surface and the blood can be identified when imaging a drop of blood on a superamphiphobic surface by LSCM (Figure 1.20b).

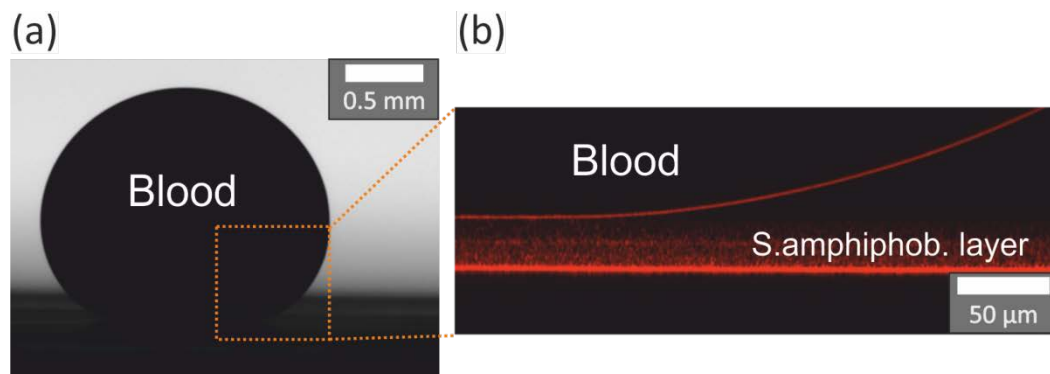


Figure 1.20 (a) A drop of heparinized whole human blood deposited on a superamphiphobic surface. The diameter of the drop of blood is ca. 3 mm. (b) Vertical cross-section of a blood drop on a superamphiphobic layer imaged by confocal microscopy in reflection mode. Macmillan Publishers Ltd., Nature Publishing Group: Adapted from Nat. Comm. Paven, M., et al., Super liquid-repellent gas membranes for carbon dioxide capture and heart-lung machines, 4, copyright 2013.

Various protocols exist for quantitative analysis of proteins. The adhesion of proteins to superamphiphobic surfaces can be quantified after contact of a superamphiphobic substrate and blood for several hours. After removing the blood by tilting the wells no residuals were detected by eye (Figure 1.21).



Figure 1.21 Heparinized blood was incubated for 6 h in a superamphiphobic well and removed afterwards by tilting. Macmillan Publishers Ltd., Nature Publishing Group: Nat. Comm. Paven, M., et al., Super liquid-repellent gas membranes for carbon dioxide capture and heart-lung machines, 4, copyright 2013.

The area of the wells which were in direct contact with the supernatant blood were analyzed using the Pierce 660 nm Protein Assay Kit. As a result, one obtained the total amount of adhered protein per cm^2 of analysed mesh. Superamphiphobic meshes without any contact to blood were equally analyzed and served as control samples. Also, a superamphiphobic surface was exposed to a circulating flow of whole human blood for 3 h. After the flow cell was opened, no blood was found on the membrane. In contrast, a Teflon membrane used as reference was covered by blood (Figure 1.22b). Figure 1.22a shows the average value of protein adsorption for each surface type.

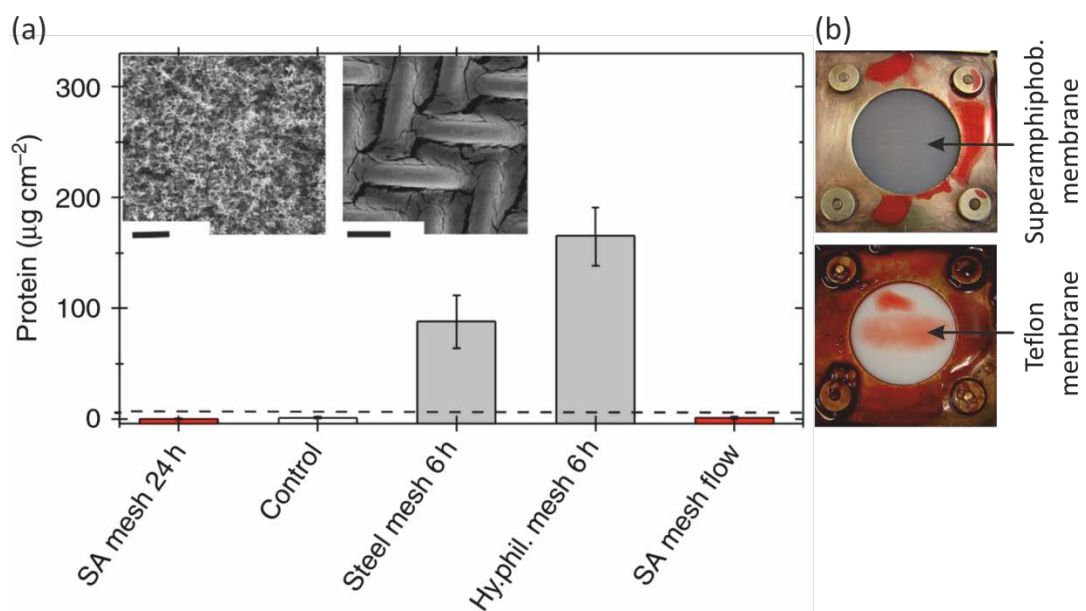


Figure 1.22 (a) Protein adhesion in $\mu\text{g}/\text{cm}^2$ for metal, hydrophilic and superamphiphobic (SA) meshes at different time points, respectively. The indicated detection limit (dashed line) was derived from the known sensibility limit of the Pierce 660 nm Test. Error bars are based upon the root mean square deviation. (b) Images of flow cell equipped with superamphiphobic (top) and Teflon membrane

(bottom) after being exposed to a flow of heparinized blood for 3 h. Macmillan Publishers Ltd., Nature Publishing Group: Adapted from Nat. Comm. Paven, M., et al., Super liquid-repellent gas membranes for carbon dioxide capture and heart-lung machines, 4, copyright 2013.

In contrast to steel and hydrophilic meshes, superamphiphobic meshes incubated for 24 h, superamphiphobic meshes exposed to blood flow for 3 h and control meshes were below the detection limit of $6.25 \mu\text{g}/\text{cm}^2$. Also, no cells or other blood components were found by electron microscopy on a superamphiphobic surface incubate for 48 h (Figure 1.22a, left inset). In contrast, Figure 1.22a, right inset shows a steel mesh exposed to 2 h of human blood.

1.2.5 Superamphiphobic Membranes.

So far, most superhydrophobic and superamphiphobic layers were prepared on solid surface. Few techniques exist to coat meshes or to fabricate superamphiphobic surfaces that are gas permeable. Superamphiphobic meshes can be used as highly efficient contactor membranes for gas exchange between a liquid and a gas phase, i.e. O_2 enrichment of haemoglobin, or for self-cleaning textiles (Figure 1.23)^{75, 106}. Superamphiphobic membranes are less sensitive to membrane wetting and plugging than conventional materials.

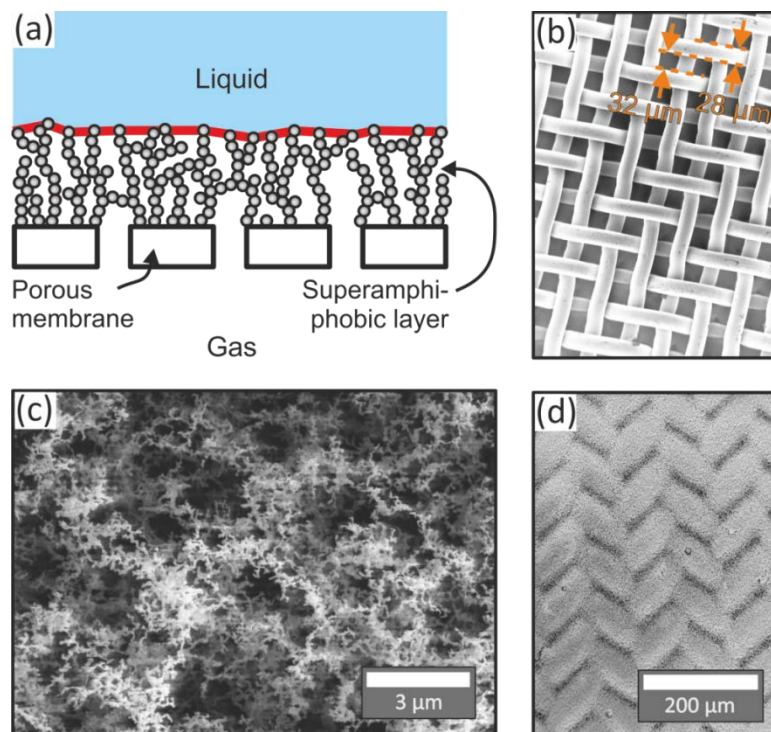


Figure 1.23 a) Schematic drawing of a superamphiphobic membrane. b) SEM of a blank stainless steel metal mesh. c) Stainless steel mesh coated with a superamphiphobic layer (scale bar: 200 μm). d) Magnification of the

superamphiphobic layer (scale bar: 3 μm). Macmillan Publishers Ltd., Nature Publishing Group: Adapted from Nat. Comm. Paven, M., et al., Super liquid-repellent gas membranes for carbon dioxide capture and heart-lung machines, 4, copyright 2013.

Typically, gas contactor membranes consist of nonporous, mostly polymeric membranes, supported liquid membranes or porous membranes¹⁰⁷⁻¹⁰⁹. Gas and liquid are separated by the contactor membrane. Gas molecules diffuse from the feed to the permeate side of the membrane, along a concentration gradient. The efficiency of the membrane is defined by the mass transfer coefficient K .^{110, 111} The mass transfer coefficient is defined as the amount of gas transferred per time \dot{n} and per unit area A divided by the driving concentration difference Δc : $K = \dot{n}/(A \Delta c)$.

As one example we demonstrated the oxygenation of blood. Therefore, first a 1.2% solution of whole human blood stabilized with lithium-heparin as anticoagulant in phosphate buffer saline (PBS, Dulbecco's PBS) was deoxygenized by bubbling a continuous stream of nitrogen through the solution for 30 min at 37 °C; blood was diluted to reach a high sensitivity in the UV/VIS absorption spectrometer. Deoxygenated blood in PBS was transferred into the reservoir of the setup (Fig. 25a) under nitrogen. We continuously recorded UV/VIS absorption spectra, while diluted blood circulated for 16 min under nitrogen atmosphere until oxygen was introduced into the gas box at a flow rate of 0.7 L/min. Spectra measured at $t = 0$ min and $t = 45$ min demonstrate that pumped blood in PBS was successfully oxygenated.

Using superamphiphobic membranes for medical application, as for the oxygenation of blood, it needs to be ensured that the coating preserves its long time stability. In particular, breaking off of parts of the top most region of the coating needs to be prevented as otherwise fluorinated nanoparticles might enter the bloodstream. This is still remains a challenge.

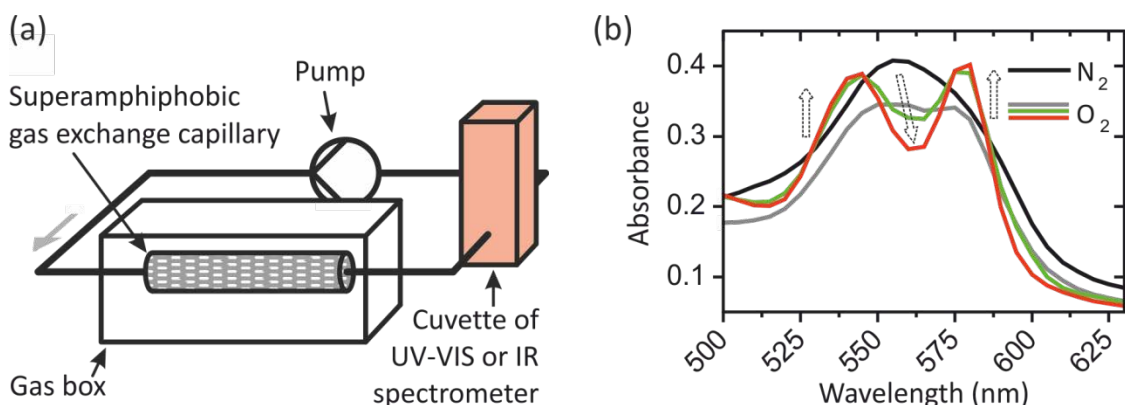


Figure 1.24 (a) Sketch of a setup used to measure gas exchange. A gas box contained a flow cell equipped with superamphiphobic membranes. Sodium hydroxide solution or deoxygenized blood was pumped through the flow cell and

UV-Vis spectra were subsequently recorded to monitor the gas exchange. (b) Absorbance spectra of 1.2% deoxygenated blood before (black) and its subsequent change while being exposed to oxygen (grey to red). The mono-peak of deoxygenated blood (black, N₂) transformed into the characteristic double-peak of oxygenated blood at 560 nm (grey to red, O₂), proving successful exchange. Macmillan Publishers Ltd., Nature Publishing Group: Adapted from Nat. Comm. Paven, M., et al., Super liquid-repellent gas membranes for carbon dioxide capture and heart-lung machines, 4, copyright 2013.

1.2.6 Fog harvesting

Water supply in arid regions is commonly performed by desalination. More than 15000 desalination plants are installed and operate worldwide ¹¹². The installed capacity around the Mediterranean is about 12×10^6 m³/day ¹¹³, of which 70% is used for irrigation. Water desalination suffers from high operational energy consumption. Depending on the input water salinity, the specific energy requirement is 2-3 kWh/m³ H₂O, corresponding to a fingerprint of 1.4 to 1.8 kg CO₂ per cubic meter of produced water ¹¹⁴. Lately, the possibilities to collect water directly from humid atmospheric air or fog have been investigated. Fog forms when humid air is cooled below its dew point, e.g. when it moves upward. Foggy air contains 0.05-0.5 g H₂O/m³. Thus, a 40 m² surface could ideally collect up to 1700 L/day at a wind speed of 1 m/s. "Fog harvesting" is meant to be a process in which water is collected from supersaturated humid air, mist or fog using 'traps' made of engineered materials (Figure 1.24) ^{115, 116}. Tiny water droplets are taken along by wind until they hit the traps, adhere on the surface and grow by coalescence or condensation until they reach a certain size and roll-off. This water is collected.

The idea of collecting water from air in arid areas originates from the ability of beetles (*Stenocara gracilipes*) in the Namib Desert on the west coast of Africa to drink water from the morning dew ¹¹⁷. The beetle's surface is composed of alternating hydrophilic and hydrophobic areas. The hydrophilic parts collect the fog and the hydrophobic areas repel the condensed drops as soon as they reach a certain size ¹¹⁸.

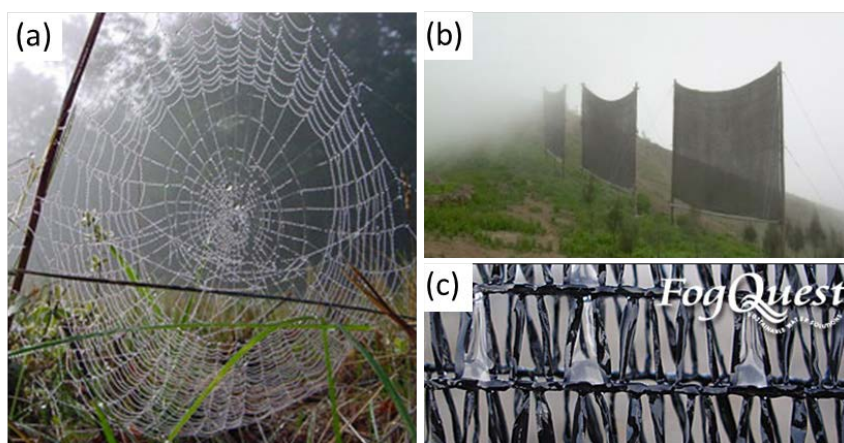


Figure 1.25 (a) Water drops on a spider net. Reproduced from http://www.rsc.org/images/Spider_Web_250_tcm18-209682.jpg. (b) The charitable organization FogQuest installed one of the first fog harvesting devices in Chungungo, Chile in the Atacama Desert in 1992. Six years later with the help of 80 fog collectors, village residents were enjoying an average of 10,000-15,000 liters of fresh drinking water each day, which amounts to an average of 35 liters per person. Reproduced from <http://www.climateprep.org>. Copyright by Anne Lummerich (c) At the moment the meshes are made of simple polymer fibers. Reproduced from <http://www.fogquest.org/>.

Currently meshes collect only a small fraction of the air humidity (Figure 1.246a, b). By facilitating the mechanisms of water condensation and drop collection on solid surfaces and in particular the subsequent droplet roll-off the efficiency of fog harvesting will be increased. McKinley et al. have intensively investigated the optimum design of the mesh with respect of their hydrophobicity, wire thickness and spacing¹¹⁹. To maximize the efficiency for fog harvesting efficient condensation of water molecules or water droplets on the surface of the mesh is needed¹¹⁹⁻¹²¹. Simultaneously, easy roll-off of the drops is required to prevent evaporation of drops that stick to the mesh. Therefore, surfaces and fabrics that imitate the structure of the *Stenocara gracilipes* beetle have been synthesized¹²². Hydrophilicity favors condensation, however inhibits droplet roll-off (Figure 1.25 grey spots). On the contrary, superhydrophobicity inhibits condensation, while favoring roll off. Still it is unclear which material and which topography combine hydrophilicity with superhydrophobicity in a way that optimizes water collection performance. However, no cheap procedure of sufficient mechanical stability has been designed yet, providing large scale production. Furthermore, the optimized meshes need to be cheap, mechanically stable, and UV resistant.

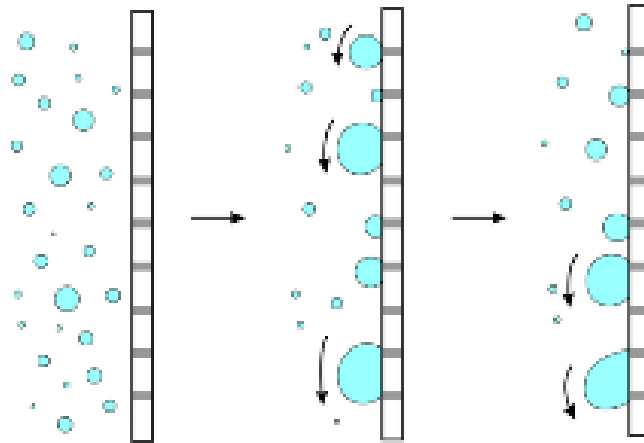


Figure 1.26 Sketch of adhesion and roll-off of water drops on a surface possessing hydrophilic (grey) and superhydrophobic regions.

1.3 Challenges

For industrial applications the methods to fabricate superhydrophobic or superamphiphobic surfaces need to be reproducible, cheap and scalable. Compared to superhydrophobic surfaces, it is much more demanding to fabricate overhang structures that are required to achieve superamphiphobicity. The precise control of surface protrusions' spacing, size and geometry is crucial to establish a stable Cassie state and to achieve high liquid repellency. The lower the surface tension of the liquid becomes the more careful these parameters need to be chosen. The durability of the superhydrophobic or –amphiphobic coating should be high. The coating should resist UV exposure, acidic and basic solutions and common solvents. This depends mostly on the chemical nature of the coating's materials. The most challenging factor for industrial application is the long-term mechanical stability of the surface. In general, overhang structures show weaker mechanical resistance towards shearing than pillars or pyramidal shapes. During abrasion, not only the structure will change its geometry, but also the surface chemistry may change from hydrophobic to hydrophilic. This increases adhesion and therefore increases contact angle hysteresis.

ACKNOWLEDGMENTS

Financial support from ERC grant SuPro and COST1106 is gratefully acknowledged.

1. T. Young, *Philosophical Transactions Royal Society London*, 1805, **95**, 65-87.
2. C. W. Extrand, *Langmuir*, 2006, **22**, 1711-1714.
3. T. Nishino, M. Meguro, K. Nakamae, M. Matsushita and Y. Ueda, *Langmuir*, 1999, **15**, 4321-4323.
4. H. J. Butt, K. Graf and M. Kappl, *Physics and Chemistry of Interfaces*, WILEY-VCH Verlag GmbH & Co. KGaA, Weinheim, 2006.
5. R. N. Wenzel, *Industrial and Engineering Chemistry*, 1936, **28**, 988-994.
6. A. Lafuma and D. Quere, *Nat. Mater.*, 2003, **2**, 457-460.
7. A. B. D. Cassie and S. Baxter, *T Faraday Soc*, 1944, **40**, 0546-0550.
8. E. L. Decker and S. Garoff, *Langmuir*, 1997, **13**, 6321-6332.
9. P. Papadopoulos, X. Deng, L. Mammen, D. M. Drotlef, G. Battagliarin, C. Li, K. Müllen, K. Landfester, A. del Campo, H.-J. Butt and D. Vollmer, *Langmuir*, 2012, **28**, 8392-8398.
10. L. Mammen, K. Bley, P. Papadopoulos, F. Schellenberger, N. Encinas, H.-J. Butt, C. K. Weiss and D. Vollmer, *Soft Matter*, 2015, **11**, 506-515.
11. Boys, *Soap bubbles*, Society for Promoting Christian Knowledge, London, 1902.
12. T. L. Sun, L. Feng, X. F. Gao and L. Jiang, *Accounts of Chemical Research*, 2005, **38**, 644-652.
13. X. F. Gao and L. Jiang, *Nature*, 2004, **432**, 36-36.
14. C. Neinhuis and W. Barthlott, *Annals of Botany*, 1997, **79**, 667-677.
15. W. Barthlott and C. Neinhuis, *Planta*, 1997, **202**, 1-8.
16. L. C. Gao and T. J. McCarthy, *Langmuir*, 2006, **22**, 2966-2967.
17. D. K. Owens and R. C. Wendt, *J Appl Polym Sci*, 1969, **13**, 1741-1747.
18. A. M. Cao, L. L. Cao and D. Gao, *Appl Phys Lett*, 2007, **91**.
19. L. L. Cao, H. H. Hu and D. Gao, *Langmuir*, 2007, **23**, 4310-4314.
20. S. Herminghaus, *Europhys Lett*, 2000, **52**, 165-170.
21. Y. T. Cheng and D. E. Rodak, *Appl Phys Lett*, 2005, **86**.
22. W. Chen, A. Y. Fadeev, M. C. Hsieh, D. Oner, J. Youngblood and T. J. McCarthy, *Langmuir*, 1999, **15**, 3395-3399.

23. A. Tuteja, W. Choi, M. L. Ma, J. M. Mabry, S. A. Mazzella, G. C. Rutledge, G. H. McKinley and R. E. Cohen, *Science*, 2007, **318**, 1618-1622.
24. L. L. Cao, T. P. Price, M. Weiss and D. Gao, *Langmuir*, 2008, **24**, 1640-1643.
25. A. Ahuja, J. A. Taylor, V. Lifton, A. A. Sidorenko, T. R. Salamon, E. J. Lobaton, P. Kolodner and T. N. Krupenkin, *Langmuir*, 2008, **24**, 9-14.
26. X. Deng, L. Mammen, H. J. Butt and D. Vollmer, *Science*, 2012, **335**, 67-70.
27. T. L. Liu and C.-J. C. J. Kim, *Science*, 2014, **346**, 1096-1100.
28. R. Hensel, R. Helbig, S. Aland, H. G. Braun, A. Voigt, C. Neinhuis and C. Werner, *Langmuir*, 2013, **29**, 1100-1112.
29. Z. G. Guo, W. M. Liu and B. L. Su, *Journal of Colloid and Interface Science*, 2011, **353**, 335-355.
30. J. Bico, C. Marzolin and D. Quéré, *Europhys. Lett.*, 1999, **47**, 220-226.
31. D. Bartolo, F. Bouamrine, E. Verneuil, A. Buguin, P. Silberzan and S. Moulinet, *Europhys. Lett.*, 2006, **74**, 299-305.
32. C. Dorrer and J. Rühe, *Soft Matter*, 2009, **5**, 51-61.
33. C. Priest, T. W. J. Albrecht, R. Sedev and J. Ralston, *Langmuir*, 2009, **25**, 5655-5660.
34. D. Xiong, G. J. Liu, L. Z. Hong and E. J. S. Duncan, *Chem Mater*, 2011, **23**, 4357-4366.
35. A. Steele, I. Bayer and E. Loth, *Nano Lett.*, 2009, **9**, 501-505.
36. R. Dufour, M. Harnois, V. Thomy, R. Boukherroub and V. Senez, *Soft Matter*, 2011, **7**, 9380-9387.
37. T. Darmanin, F. Guittard, S. Amigoni, E. T. de Givenchy, X. Noblin, R. Kofman and F. Celestini, *Soft Matter*, 2011, **7**, 1053-1057.
38. H. J. Butt, C. Semprebon, P. Papadopoulos, D. Vollmer, M. Brinkmann and M. Ciccotti, *Soft Matter*, 2013, **9**, 418-428.
39. M. R. Flynn and J. W. M. Bush, *J. Fluid Mech.*, 2008, **608**, 275-296.
40. M. L. Blow and J. M. Yeomans, *Langmuir*, 2010, **26**, 16071-16083.
41. K. Tsujii, T. Yamamoto, T. Onda and S. Shibuichi, *Angewandte Chemie International Edition in English*, 1997, **36**, 1011-1012.
42. B. He, N. A. Patankar and J. Lee, *Langmuir*, 2003, **19**, 4999-5003.
43. E. Bormashenko, R. Pogreb, G. Whyman and M. Erlich, *Langmuir*, 2007, **23**, 6501-6503.

44. T. N. Krupenkin, J. A. Taylor, E. N. Wang, P. Kolodner, M. Hodes and T. R. Salamon, *Langmuir*, 2007, **23**, 9128-9133.
45. P. Papadopoulos, L. Mammen, X. Deng, D. Vollmer and H. J. Butt, *PNAS*, 2013, **110**, 3254–3258.
46. M. Reyssat, J. M. Yeomans and D. Quere, *Epl*, 2008, **81**.
47. D. Bartolo, F. Bouamrène, E. Verneuil, A. Buguin, P. Silberzan and S. Moulinet, *Europhys Lett*, 2006, **74**, 299-305.
48. J. F. Oliver, C. Huh and S. G. Mason, *Journal of Colloid and Interface Science*, 1977, **59**, 568-581.
49. A. ElSherbini and A. Jacobi, *J. Coll. Interf. Sci.*, 2006, **299**, 841-849.
50. T. Verho, C. Bower, P. Andrew, S. Franssila, O. Ikkala and R. H. A. Ras, *Adv Mater*, 2011, **23**, 673-678.
51. C.-H. Xue and J.-Z. Ma, *Journal of Materials Chemistry A*, 2013, **1**, 4146-4161.
52. D. Ebert and B. Bhushan, *Journal of Colloid and Interface Science*, 2012, **368**, 584-591.
53. J. Groten and J. Rühle, *Langmuir*, 2013, **29**, 3765-3772.
54. Y. C. Jung and B. Bhushan, *ACS Nano*, 2009, **3**, 4155-4163.
55. B. P. Dyett, A. H. Wu and R. N. Lamb, *ACS Applied Materials & Interfaces*, 2014, **6**, 18380-18394.
56. E. J. Lee, J. J. Kim and S. O. Cho, *Langmuir*, 2010, **26**, 3024-3030.
57. X. Deng, L. Mammen, Y. F. Zhao, P. Lellig, K. Mullen, C. Li, H. J. Butt and D. Vollmer, *Adv Mater*, 2011, **23**, 2962-+.
58. Y. Wu, M. Bekke, Y. Inoue, H. Sugimura, H. Kitaguchi, C. Liu and O. Takai, *Thin Solid Films*, 2004, **457**, 122-127.
59. H. Wang, Y. Xue, J. Ding, L. Feng, X. Wang and T. Lin, *Angewandte Chemie International Edition*, 2011, **50**, 11433-11436.
60. P. S. Brown and B. Bhushan, *Sci. Rep.*, 2015, **5**.
61. X. Shi, T. A. Nguyen, Z. Suo, J. Wu, J. Gong and R. Avci, *Surface and Coatings Technology*, 2012, **206**, 3700-3713.
62. M. L. B. Palacio and B. Bhushan, *Materials Characterization*, 2013, **78**, 1-20.
63. B. Bhushan, *Wear*, 1999, **225–229, Part 1**, 465-492.
64. X. Feng and L. Jiang, *Advanced Materials*, 2006, **18**, 3063-3078.
65. B. Bhushan and Y. C. Jung, *Prog. Mat. Sci.*, 2011, **56**, 1-108.

66. G. McHale, M. I. Newton and N. J. Shirtcliffe, *Soft Matter*, 2010, **6**, 714-719.
67. J. P. Rothstein, in *Annual Review of Fluid Mechanics*, Annual Reviews, Palo Alto, 2010, vol. 42, pp. 89-109.
68. P. Joseph, C. Cottin-Bizonne, J. M. Benoit, C. Ybert, C. Journet, P. Tabeling and L. Bocquet, *Physical Review Letters*, 2006, **97**.
69. R. B. Pernites, C. M. Santos, M. Maldonado, R. R. Ponnappati, D. F. Rodrigues and R. C. Advincula, *Chemistry of Materials*, 2012, **24**, 870-880.
70. Y. Koc, A. J. de Mello, G. McHale, M. I. Newton, P. Roach and N. J. Shirtcliffe, *Lab on a Chip*, 2008, **8**, 582-586.
71. C. Pang, G. Y. Lee, T. I. Kim, S. M. Kim, H. N. Kim, S. H. Ahn and K. Y. Suh, *Nature Materials*, 2012, **11**, 795-801.
72. N. Andreeva, T. Ishizaki, P. Baroch and N. Saito, *Sensors and Actuators B-Chemical*, 2012, **164**, 15-21.
73. Y. Gao, T. Chen, S. Yamamoto, T. Miyashita and M. Mitsuishi, *Acs Applied Materials & Interfaces*, 2015, **7**, 3468-3472.
74. H. F. Hoefnagels, D. Wu, G. de With and W. Ming, *Langmuir*, 2007, **23**, 13158-13163.
75. G. R. J. Artus, J. Zimmermann, F. A. Reifler, S. A. Brewer and S. Seeger, *Applied Surface Science*, 2012, **258**, 3835-3840.
76. M. Yu, G. Gu, W.-D. Meng and F.-L. Qing, *Applied Surface Science*, 2007, **253**, 3669-3673.
77. M. Paven, P. Papadopoulos, S. Schoettler, X. Deng, V. Mailaender, D. Vollmer and H.-J. Butt, *Nat. Comm.*, 2013, **4**.
78. X. Deng, M. Paven, P. Papadopoulos, M. Ye, S. Wu, T. Schuster, M. Klapper, D. Vollmer and H.-J. Butt, *Angewandte Chemie-International Edition*, 2013, **52**, 11286-11289.
79. V. Rastogi, S. Melle, O. G. Calderon, A. A. Garcia, M. Marquez and O. D. Velev, *Advanced Materials*, 2008, **20**, 4263-4268.
80. V. Rastogi, A. A. Garcia, M. Marquez and O. D. Velev, *Macromolecular Rapid Communications*, 2010, **31**, 190-195.
81. B. Comiskey, J. D. Albert, H. Yoshizawa and J. Jacobson, *Nature*, 1998, **394**, 253-255.
82. J. Du and R. K. O'Reilly, *Chemical Society Reviews*, 2011, **40**, 2402-2416.

83. K. Matyjaszewski and T. P. Davis, *Handbook of radical polymerization*, Wiley Online Library, 2002.
84. D. Dendukuri and P. S. Doyle, *Adv Mater*, 2009, **21**, 4071-4086.
85. M. Sperling, O. D. Veleev and M. Gradzielski, *Angew Chem Int Edit*, 2014, **53**, 586-590.
86. A. G. Marin, H. Gelderblom, A. Susarrey-Arce, A. van Houselt, L. Lefferts, J. G. E. Gardeniers, D. Lohse and J. H. Snoeijer, *Proceedings of the National Academy of Sciences of the United States of America*, 2012, **109**, 16455-16458.
87. K. Ikemura and T. Endo, *Dental Materials Journal*, 2010, **29**, 481-501.
88. R. A. N. Chmielewski and J. F. Frank, *Journal of Food Protection*, 2004, **67**, 2712-2718.
89. R. M. Klevens, J. R. Edwards, C. L. Richards, Jr., T. C. Horan, R. P. Gaynes, D. A. Pollock and D. M. Cardo, *Public Health Reports*, 2007, **122**, 160-166.
90. J. W. Costerton, P. S. Stewart and E. P. Greenberg, *Science*, 1999, **284**, 1318-1322.
91. J. N. Wilking, T. E. Angelini, A. Seminara, M. P. Brenner and D. A. Weitz, *Mrs Bulletin*, 2011, **36**, 385-391.
92. X. Chen and H. J. Schluesener, *Toxicology Letters*, 2008, **176**, 1-12.
93. P. S. Stewart and J. W. Costerton, *Lancet*, 2001, **358**, 135-138.
94. I. Banerjee, R. C. Pangule and R. S. Kane, *Adv. Mat.*, 2011, **23**, 690-718.
95. K. D. Park, Y. S. Kim, D. K. Han, Y. H. Kim, E. H. B. Lee, H. Suh and K. S. Choi, *Biomaterials*, 1998, **19**, 851-859.
96. S. Mazumder, J. O. Falkinham, A. M. Dietrich and I. K. Puri, *Biofouling*, 2010, **26**, 333-339.
97. D. C. Leslie, A. Waterhouse, J. B. Berthet, T. M. Valentin, A. L. Watters, A. Jain, P. Kim, B. D. Hatton, A. Nedder, K. Donovan, E. H. Super, C. Howell, C. P. Johnson, T. L. Vu, D. E. Bolgen, S. Rifai, A. R. Hansen, M. Aizenberg, M. Super, J. Aizenberg and D. E. Ingber, *Nat. Biotech.*, 2014, **32**, 1134-1140.
98. R. J. Crawford, H. K. Webb, T. Vi Khanh, J. Hasan and E. P. Ivanova, *Advances in Colloid and Interface Science*, 2012, **179**, 142-149.
99. J. Genzer and K. Efimenko, *Biofouling*, 2006, **22**, 339-360.
100. X. Hou, X. Wang, Q. Zhu, J. Bao, C. Mao, L. Jiang and J. Shen, *Colloids and Surfaces B-Biointerfaces*, 2010, **80**, 247-250.

101. H. Fan, P. Chen, R. Qi, J. Zhai, J. Wang, L. Chen, L. Chen, Q. Sun, Y. Song, D. Han and L. Jiang, *Small*, 2009, **5**, 2144-2148.
102. B. J. Privett, J. Youn, S. A. Hong, J. Lee, J. Han, J. H. Shin and M. H. Schoenfish, *Langmuir*, 2011, **27**, 9597-9601.
103. G. J. Toes, K. W. van Muiswinkel, W. van Oeveren, A. J. H. Suurmeijer, W. Timens, I. Stokroos and J. van den Dungen, *Biomaterials*, 2002, **23**, 255-262.
104. T. Ishizaki, N. Saito and O. Takai, *Langmuir*, 2010, **26**, 8147-8154.
105. S. M. Oliveira, W. Song, N. M. Alves and J. F. Mano, *Soft Matter*, 2011, **7**, 8932-8941.
106. B. Leng, Z. Shao, G. de With and W. Ming, *Langmuir*, 2009, **25**, 2456-2460.
107. M. C. Yang and E. L. Cussler, *AIChE J.*, 1986, **32**, 1910-1916.
108. R. Prasad and K. K. Sirkar, *AIChE J.*, 1988, **34**, 177-188.
109. A. Gabelman and S. T. Hwang, *J. Membrane Sci.*, 1999, **159**, 61-106.
110. W. D. Zhang, J. A. Li, G. Chen, W. You, Y. Jiang and W. Sun, *Ind. Eng. Chem. Res.*, 2010, **49**, 6641-6648.
111. C. S. Feng, R. Wang, H. Y. Zhang and L. Shi, *J. Appl. Polymer Sci.*, 2011, **119**, 1259-1267.
112. L. F. Greenlee, D. F. Lawler, B. D. Freeman, B. Marrot and P. Moulin, *Water Res*, 2009, **43**, 2317-2348.
113. J. C. Cuenca, *Report on the Water Desalination Status in the Mediterranean Countries*, Instituto Murciano de Investigación y Desarrollo Agroalimentario Murcia, Spain, 2012.
114. M. Elimelech and W. A. Phillip, *Science*, 2011, **333**, 712-717.
115. J. Olivier, *Water Sa*, 2002, **28**, 349-360.
116. S. A. Abdul-Wahab, H. Al-Hinai, K. A. Al-Najar and M. S. Al-Kalbani, *Environmental Engineering Science*, 2007, **24**, 446-456.
117. T. Norgaard and M. Dacke, *Frontiers in zoology*, 2010, **7**, 23.
118. A. R. Parker and C. R. Lawrence, *Nature*, 2001, **414**, 33-34.
119. K.-C. Park, S. S. Chhatre, S. Srinivasan, R. E. Cohen and G. H. McKinley, *Langmuir*, 2013, **29**, 13269-13277.
120. M. A. K. Azad, D. Ellerbrok, W. Barthlott and K. Koch, *Bioinspiration & Biomimetics*, 2015, **10**.
121. L. Zhang, J. Wu, M. N. Hedhili, X. Yang and P. Wang, *Journal of Materials Chemistry A*, 2015, **3**, 2844-2852.

122. C. Dorrer and J. Ruhe, *Langmuir*, 2008, **24**, 6154-6158.